Department of Physics
Faculty of Science
University of Helsinki, Finland

Polarization studies in electromagnetic scattering by small Solar-system particles

Jani Tyynelä

Academic dissertation

To be presented, with the permission of the Faculty of Science of the University of Helsinki, for public criticism in Auditorium E204 of the Physicum building on 3rd November, 2011, at 12 o'clock noon.

Cover:
Degree of linear polarization for wavelength-scale spheroidal particles (top image). The internal field contribution to the scattered far field for the spheroidal particles near the backscattering direction (bottom images).

ISSN-L 1799-3024
ISSN 1799-3024 (printed version)
ISSN 1799-3032 (pdf version)
ISBN 978-952-10-7070-9 (printed version)
ISBN 978-952-10-7071-6 (pdf version)
http://www.ethesis.helsinki.fi
Yliopistopaino
Helsinki 2011

Abstract

In remote-sensing studies, particles that are comparable to the wavelength exhibit characteristic features in electromagnetic scattering, especially in the degree of linear polarization. These features vary with the physical properties of the particles, such as shape, size, refractive index, and orientation. In the thesis, the direct problem of computing the unknown scattered quantities using the known properties of the particles and the incident radiation is solved at both optical and radar spectral regions in a unique way.

The internal electromagnetic fields of wavelength-scale particles are analyzed by using both novel and established methods to show how the internal fields are related to the scattered fields in the far zone. This is achieved by using the tools and methods that were developed specifically to reveal the internal field structure of particles and to study the mechanisms that relate the structure to the scattering characteristics of those particles. It is shown that, for spherical particles, the internal field is a combination of a forward propagating wave with the apparent wavelength determined by the refractive index of the particle, and a standing wave pattern with the apparent wavelength the same as for the incident wave. Due to the surface curvature and dielectric nature of the particle, the incident wave front undergoes a phase shift, and the resulting internal wave is focused mostly at the forward part of the particle similar to an optical lens. This focusing is also seen for irregular particles. It is concluded that, for both spherical and nonspherical particles, the interference at the far field between the partial waves that originate from these concentrated areas in the particle interior, is responsible for the specific polarization features that are common for wavelength-scale particles, such as negative values and local extrema in the degree of linear polarization, asymmetry of the phase function, and enhancement of intensity near the backscattering direction.

The papers presented in this thesis solve the direct problem for particles with both simple and irregular shapes to demonstrate that these interference mechanisms are common for all dielectric wavelength-scale particles. Furthermore, it is shown that these mechanisms can be applied to both regolith particles in the optical wavelengths and hydrometeors at microwave frequencies. An advantage from this kind of study is that it does not matter whether the observation is active (e.g., polarimetric radar) or passive (e.g., optical telescope). In both cases, the internal field is computed for two mutually perpendicular incident polarizations, so that the polarization characteristics can then be analyzed according to the relation between these fields and the scattered far field.

Acknowledgements

During the years I have been working on the thesis, there have been several people that provided guidance and support for me. First, I want to thank professor Karri Muinonen who convinced me that there might actually be something interesting in the internal fields of particles. Over the years, he has been the one to push me deeper into light scattering studies and showed me, that the deeper I go, the less I actually know.

Another person who has had a great influence on me is doctor Timo Nousiainen. When I expanded my research interest into atmospheric sciences, he helped me to find my place in this field, which at first seemed unfamiliar to me. I have also enjoyed our endless discussions on topics that may not be relevant for this study, but that have kept me partly sane from staying long hours in front of the computer screen. Doctor Evgenij Zubko introduced me to the discrete-dipole approximation, which I have used regurarly ever since. Doctor Dmitri Moisseev has been my backbone in radar-related studies. I have been lucky to have four excellent advisors in my thesis studies.

I am grateful for the Academy of Finland, which has funded most of my studies, and the Center for Scientific Computing, which has provided me access to their superclusters. I have probably used more CPU-hours than done real working hours.

I want to thank my other colleagues in the planetary system and the atmospheric radiation research groups for constant support. Especially Antti Penttilä and Jussi Leinonen, who I consider to be my fellow computation accomplishers. There are many former colleagues who have contributed to this study in small parts. Thank you all!

Lastly, I thank my family for helping me to get my mind out of work-related stuff. It has been valuable during more difficult times.

List of papers

I Muinonen, K., Zubko, E., **Tyynelä, J.**, Shkuratov, Yu. G., and Videen, G., 2007. Light scattering by Gaussian random particles with discrete-dipole approximation. *Journal of Quantitative Spectroscopy and Radiative Transfer* **106**, 360–377

II **Tyynelä, J.**, Zubko, E., Videen, G., and Muinonen, K., 2007. Interrelating angular scattering characteristics to internal electric fields for wavelength-scale spherical particles. *Journal of Quantitative Spectroscopy and Radiative Transfer* **106**, 520–534

III **Tyynelä, J.**, Muinonen, K., Zubko, E., and Videen, G., 2008. Interrelating scattering characteristics to internal electric fields for Gaussian-random-sphere particles. *Journal of Quantitative Spectroscopy and Radiative Transfer* **109**, 2207–2218

IV **Tyynelä, J.**, Zubko, E., Muinonen, K., and Videen, G., 2010. Interpretation of single-particle negative polarization at intermediate scattering angles. *Applied Optics* **49**, 5284–5296

V Muinonen, K., **Tyynelä, J.**, Zubko, E., Lindqvist, H., Penttilä, A., and Videen, G., 2011. Polarization of light backscattered by small particles. *Journal of Quantitative Spectroscopy and Radiative Transfer*, **112**, 2193–2212

VI **Tyynelä, J.**, Nousiainen, T., Göke, S., and Muinonen, K., 2009. Modeling C-band single scattering properties of hydrometeors using discrete-dipole approximation and T-matrix method. *Journal of Quantitative Spectroscopy and Radiative Transfer* **110**, 1654–1664

VII **Tyynelä, J.**, Leinonen, J., Moisseev, D., and Nousiainen, T., 2011. Radar backscattering from snowflakes: comparison of fractal, aggregate, and soft-spheroid models. *Journal of Atmospheric and Oceanic Technology*, in press

Acronyms

2D-P Two-dimensional stereo probe

AD Agglomerated debris

BSA Backscattering alignment

CBM Coherent-backscattering mechanism

CIPG Cloud-particle imager (G version)

DDA Discrete-dipole approximation

EMA Effective-medium approximation

FCD Filtered coupled dipole

FSA Forward-scattering alignment

IEB Intensity-enhancement branch

GOA Geometric optics approximation

GRS Gaussian random sphere

$\mathbf{LDR}_{vh}$ Linear depolarization ratio

LDR Lattice dispersion relation

LPVEx Light precipitation validation experiment

M-G Maxwell-Garnett

NPB Negative-polarization branch

RGA Rayleigh-Gans approximation

TMM T-Matrix method

Contents

1 Introduction

Active and passive remote sensing using electromagnetic radiation is a large area of research ranging from nano-scale particles to surfaces of celestial bodies, and from the gamma rays to radio frequencies. However, the interaction of electromagnetic radiation with the matter can be characterized with only a few quantities: the size of the object compared to the wavelength of the radiation, the refractive index of the object relative to the surrounding medium, the geometric shape of the object, and the orientation of the object relative to the incoming radiation. Depending on the particular area of research, these characteristics can have quite limited variation in reality. It is therefore feasible to make assumptions about the physical properties of the objects being observed, and model the interaction of the electromagnetic radiation with the objects. This is the direct problem. In the inverse problem, the physical properties of the objects are constrained from remote-sensing observations. However, inverse problems can be ill-posed, especially without any knowledge of the *in-situ* environment. The direct problem can be used to get information about the mechanisms that govern the interaction. Once the mechanisms are known, solving the inverse problem can be improved.

1.1 Regolith particles

Regolith is the topmost layer of loose matter on terrestrial bodies that covers solid rock. It consists of irregular rock, mineral, and glassy fragments. The physical properties of single particles vary within planets, moons, and asteroids, but they are usually dielectric in nature at optical wavelengths. Together the regolith particles form a randomly rough, particulate, and porous medium with the average porosity, i.e., the volume fraction of the void, of about 70% at the surface. The lunar regolith is the most studied solar-system surface outside the Earth. During the Apollo missions about 382 kg of surface samples were returned to the Earth for study. The average diameter of the lunar regolith particles is between 60-80 μm. In absence of real samples, analog regolith particles are usually used for measurements. Analog particles must have statistically similar physical properties as real samples. Example images from the scanning-electron microscope for regolith analog particles for the Moon and Mercury are shown in Fig. 1.

At optical wavelengths, the regoliths of atmosphereless bodies can be studied with both ground-based and space-based telescopes. Depending on the physical properties of the surface, the observed signal originates from a varying combination of single and multiple scattering of sunlight from the surface. Generally, the brighter a surface is, the more contribution from multiple scattering relative to single scattering. At microwave frequencies, the regoliths are usually studied with either passive radiometers to reveal thermal distributions, or active synthetic-aperture radars aboard satellites that can penetrate deeper, and be used to map sub-surface layers.

Polarimetric measurements can be made with both optical telescopes and radars. Optical telescopes are passive devices that observe the scattered sunlight, which is typically only weakly polarized. By using polarizers and other optical elements in front of the receiver, the polarized components of the scattered wave can be measured. Radars, on the other hand, are active devices and transmit radar signals that are polarized in a specific way. The backscattered radar signal can then be received at different polarization channels to obtain the polarized components of the scattered wave.

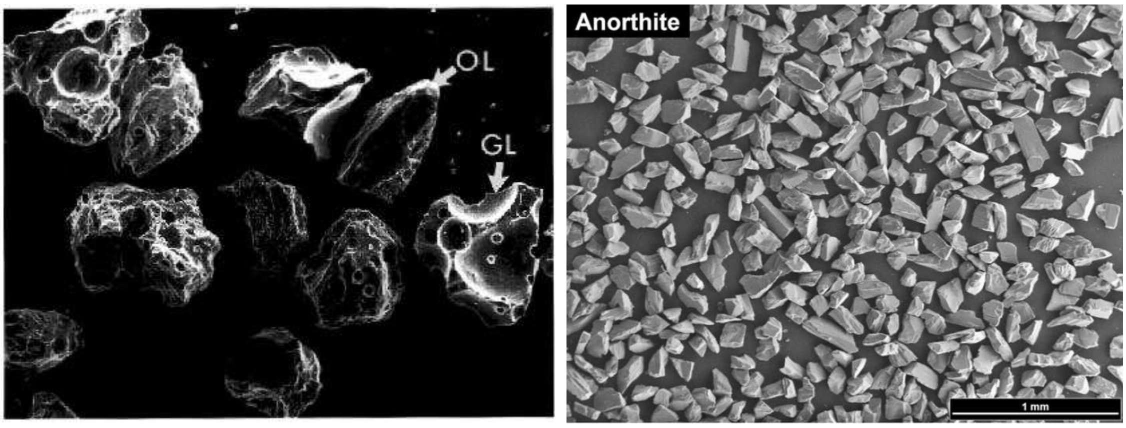

Figure 1: Scanning-electron microscope images of regolith analog particles for the Moon (left) and for Mercury (right). The images are from McKay et al. (1993) and Helbert et al. (2007). The frame width for the image on the left is 900 μm. The main crystalline phases are glass (GL), olivine (OL), and plagioclase (not shown).

.

1.2 Negative polarization

The degree of linear polarization for unpolarized incident light is defined as $P = (I_\perp - I_\parallel)/(I_\perp + I_\parallel)$, where the scattered intensities $I_\perp$ and $I_\parallel$ refer to the polarized components perpendicular and parallel to the scattering plane (defined by the light source, the scatterer, and the observer), respectively. Negative polarization is produced, when the parallel component of the scattered field is larger that the perpendicular component. Particles small compared to the wavelength interact with the incoming radiation as a single electric dipole. The angular profile of the degree of linear polarization is a symmetric bell-shaped curve; positive for all scattering angles. Such polarization is called Rayleigh-like. Wavelength-scale particles, however, exhibit non-Rayleigh-like features, such as negative-polarization branches (NPBs), interference extrema at certain angles, and asymmetry between the forward and backward scattering angles. These features are present for single particles with various shapes, sizes, refractive indices, and orientations (Hansen & Travis 1974, Yanamandra-Fisher & Hanner 1999, Petrova et al. 2000). For multiple scattering by Rayleigh-like particles, NPBs and interference extrema are absent.

One of the more interesting features is negative polarization, which is most striking for symmetric particles such as spheres. Spherical particles exhibit wide and deep branches of negative polarization at all scattering angles. These features are diminished for irregular particles such as Gaussian random particles (Muinonen et al. 2007), agglomerated-debris particles (Zubko et al. 2005), fluffy particles (Lumme & Rahola 1994), and aggregates of spherical particles (Nakamura & Okamoto 1999), although some single-scattering measurements from irregular mineral particles show negative values at intermediate scattering angles (Muñoz et al. 2001). This indicates that polarimetric quantities, especially the degree of linear polarization, are sensitive to particle shape. In addition to shape, the orientation of particles can also have a profound effect on the negative polarization. This can be seen for, e.g., spheroidal particles (Asano 1983) and hexagonal ice crystals (Yang & Liou 1996).

Although irregularity and variance in size and orientation of particles tend to dampen the presence of negative polarization, it persists near the backscattering region. This region, which is typically between $150 - 180°$ scattering angles, is called NPB. NPB is common for dielectric particles. For highly absorbing irregular particles it is absent

(Zubko et al. 2009). As regoliths consist mostly of dielectric particles at wavelength-scale sizes, NPB is also observed for most atmosphereless Solar-system bodies. It has been observed for the Moon (Lyot 1929, Shkuratov et al. 1992), Mercury (Mallama et al. 2002), asteroids (Goidet-Devel et al. 1995), comets (Levasseur-Regourd et al. 1996), and the Galilean satellites of Jupiter (Rosenbush & Kiselev 2005).

When observing surfaces that consist of bright material, i.e., have a high albedo, multiple scattering must also be taken into account. This is especially true near the exact backscattering angle, which sometimes exhibits an NPB that is attributed to the coherent backscattering mechanism (CBM; Shkuratov 1989, Muinonen 1990). CBM is a multiple-scattering phenomenon associated to the interference of reciprocal waves. It manifests itself only near the backscattering direction, and it is generally observed in icy surfaces, such as Saturn's rings (Mishchenko 1993). It is also seen in regolith analog structures (Shkuratov et al. 2002), as well as in numerical computations of multiple scattering (Muinonen & Zubko 2010). Muinonen et al. (2010) presented a novel scattering model for interpreting the polarimetric phase curves for atmosphereless solar-system bodies. In the model, the single scatterers were assumed to be negatively polarizing, and were incorporated into a coherent-backscattering model. Without CBM and/or negatively polarizing single scatterers, multiple scattering does not produce negative polarization.

1.3 Hydrometeors

Hydrometeors are particles that are formed by either condensation or deposition of water vapor in the Earth's atmosphere. These include, e.g., raindrops, hailstones, snowflakes, sleet, and graupel particles. All hydrometeors are mixtures of solid ice and liquid water with specific physical properties, such as the shape and density, determined by the processes that created them. The most common processes are coalescence of small water droplets into larger drops, depositional growth of ice crystals, melting of hydrometeors during precipitation, accretion of hydrometeors by small supercooled water droplets, i.e. riming, and aggregation of ice crystals into snowflakes. The size of hydrometeors varies from micrometer-sized water droplets to centimeter-sized hailstones. The shapes vary from almost spherical droplets and symmetric ice crystals to highly irregular snowflakes.

Because of the immediate effect of precipitation on traffic and infrastructure, it is important to monitor the precipitation continuously with operational instruments, such as weather radars. Ground-based radars are beam-scanning devices used mainly for weather surveillance, while satellite radars are used for cloud studies and surface mapping. Polarimetric weather radars can be used to, e.g., estimate rainfall and snowfall rates, detect hail, classify hydrometeor types, and derive water-ice content of clouds (Atlas et al. 1953, Aydin et al. 1986, Matrosov 1998, Straka et al. 2000). The advantage of space-borne radars is that the signal attenuation by the atmosphere is diminished. One distinct feature in radar meteorology is the bright band, which is an enhancement in the backscattered signal at the melting layer (Ryde 1946, Austin & Bemis 1950, Smyth & Illingworth 1998). It is produced by the liquid-water coating of melting ice particles mainly because liquid water is highly reflective at radar frequencies, and the melted particles scatter similarly to large raindrops.

Another important area of research is hydrometeor classification based on different polarization quantities, i.e., dual-polarization radar observables, the most important being the horizontal reflectivity, the differential reflectivity, the linear depolarization ratio, the copolarized correlation coefficient, and the specific differential phase. Due to the different morphologies of hydrometeor types and the associated processes that govern their creation, their polarimetric signatures can be categorized into different, but also slightly overlapping regions. Old classification schemes used Boolean logic to determine the hydrometeor type for a given set of radar observables, but modern schemes use fuzzy logic that can also take into account measurement errors (Liu & Chandrasekar 2000).

1.4 Snowflakes

Natural ice crystals show remarkable variation in shape, and these have been classified according to the main crystal habit, which describes the overall shape of the mineral (Nakaya 1954, Magono & Lee 1966). The habit of an ice crystal, as it grows, depends on the ambient conditions in the precipitating cloud. The main quantities that govern the growth are temperature, degree of supersaturation, and the dynamics of the cloud that controls the variability of these quantities (Fig. 2). The growth process itself can be understood by the Wegener-Bergeron-Findeisen mechanism, which explains the growth of ice at the expense of supercooled water droplets in the cloud (Pruppacher & Klett 1997). Due to the hexagonal symmetry of molecular water ice, natural ice crystals also show hexagonal symmetry (Pauling 1935). However, the most abundant type of water ice in the universe is amorphous ice observed in the interstellar medium (Festou et al. 1993). The different structure of interstellar ice is mainly due to the lower temperatures and dryness of the environment compared to the Earth's atmosphere. Also, interstellar water ice is the principal component in cosmic organics, which means that usually it is not pure, but contaminated with carbon and nitrogen (Jenniskens 1993). This difference can be observed with near-infrared spectroscopy.

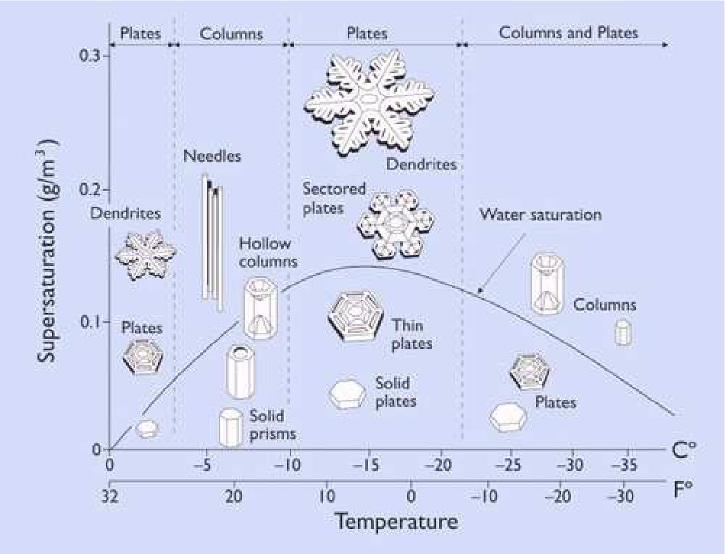

Figure 2: Morphology of ice crystals as a function of temperature and water supersaturation (Libbrecht 2005).

As the ice crystals fall, they can collide and aggregate into larger snowflakes, when the conditions are right. This process has been modeled using stochastic principles for spherical (Maruyama & Fujiyoshi 2005), dendritic (Kraus 1966), and columnar particles (Westbrook 2004). During aggregation, the snowflakes can grow up to 5–10 times larger in diameter when compared to the size of single crystals. At radar frequencies, this corresponds to an increase of 42–60 dB in radar reflectivity. Melting can further enhance the reflectivity and produce the bright band.

In free fall, ice crystals can stick to each other very loosely, which leads to a very fluffy structure for the snowflakes. Typical densities vary between 0.2–0.1 g cm^{-3} for small snowflakes to 0.05–0.01 g cm^{-3} for large snowflakes. This process is usually explained by sintering (Hobbs 1965) and mechanical interlocking (McIlveen 1992). There is a physical limit to the size of snowflakes, since the probability of breakup increases rapidly as size increases due to higher collisional damage and stress. This complicated phenomenon is explained in more detail by Göke (1999).

1.5 Modeling backscattering by snowflakes at radar frequencies

One of the advantages, when modeling falling snow, is that it is usually possible to get *in-situ* measurements using cameras and collectors. The most important physical properties that affect backscattering by snowflakes are particle mass, physical dimensions, and shape. As the polarization characteristics are sensitive to changes in these, it is crucial to constrain them in order to solve the direct scattering problem more accurately, and also to improve the inverse problem at the same time.

Different mass-diameter relations have been determined from direct measurements of snowflakes. These relations can be used to estimate the mass of snowflakes from the diameter: $m = \alpha D^{\beta}$, with α and β being the measured coefficients (Pruppacher & Klett 1997). Because it is usually assumed that snowflake aggregates are fractals to a large degree (Maruyama & Fujiyoshi 2005, Ishimoto 2008, Schmitt & Heymsfield 2010), β is the fractal dimension, which can be estimated from the images of the particles. The fractal dimension of snowflakes depends mainly on the habits of its constituent ice crystals. Values typically vary between 1.8 and 2.4 depending on the main habits. A more direct measure of mass can be done with hot plates.

Snowflake diameter is usually estimated from the images as the maximum horizontal extent of the particle. This definition is however sensitive to orientation effects, such as turbulence around the instruments. A better estimate could be the maximum extent in some arbitrary direction not fixed to any axes (Korolev & Isaac 2003). Some sample images of hydrometeors taken by the two-dimensional stereo probe (2D-P; top four rows) and the cloud-particle imager (CIPG; bottom five rows) are shown in Fig. 3. The images were taken from an aircraft at different altitudes during the light precipitation validation experiment (LPVex) near Helsinki between 15th September and 31st December 2010.

In scattering problems, the size of particles is usually expressed in size parameters $x = ka = \pi D/\lambda = \pi D f/c$ (k, λ, and f are the wave number, wavelength and frequency of the incident wave, respectively, a and D are the radius and diameter of the particle, respectively, and c the speed of light).

Ground-based weather radars usually operate at C (5.6 GHz) and S (2.7 GHz) -bands, which means that the maximum size parameters of snowflakes (with the maximum diameter D_{max} usually between 1 and 25 mm) vary between $x = 0.06$–1.5 at the C band and $x = 0.03$–0.7 at the S band. At these radar frequencies, even simple scattering models can provide reasonably good estimates for the backscattering properties. Space-based radars operate at Ku (13.6 GHz), Ka (35.6 GHz), and W (94 GHz) -bands. The corresponding size parameters vary between $x = 0.14$–3.6 at the Ku band, $x = 0.37$–9.3 at the Ka band, and $x = 1.0$–24.6 at the W band. The largest snowflakes are not seen by these instruments due to the higher attenuation through the atmosphere at higher frequencies. Despite this restriction, simple models can fail to estimate the backscattering quantities at these frequencies. The particle shape starts to dominate backscattering as the size reaches the wavelength scale.

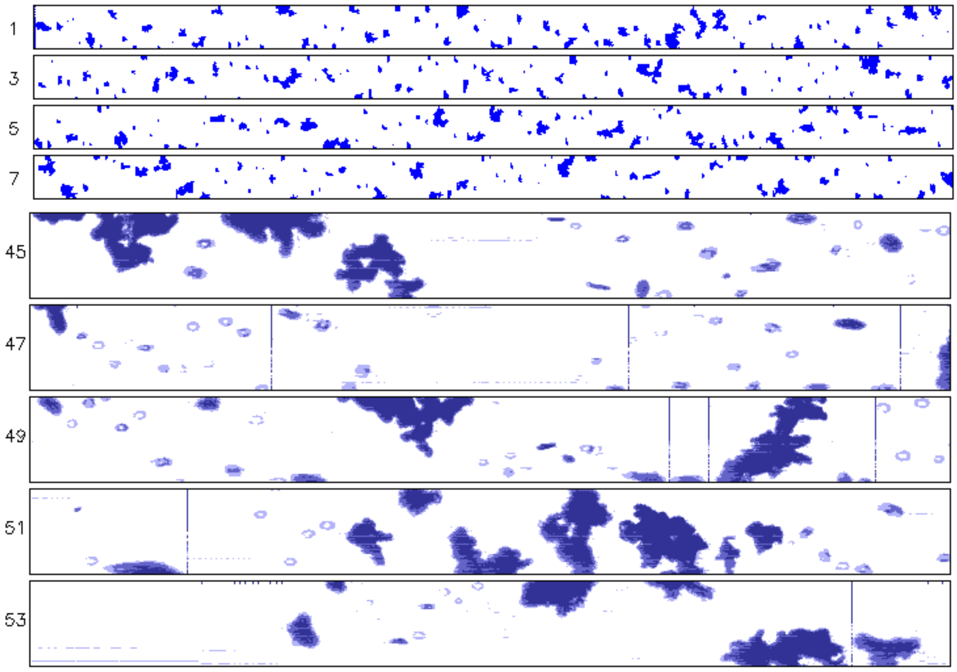

Figure 3: Top four rows are shadow images taken by the 2D-P stereo probe (resolution 200 μm/pixel), and the bottom five rows are shadow images taken by the CIPG cloud-particle imager (resolution 25 μm/pixel) during the LPVex field campaign near Helsinki (15 Sep - 31 Dec, 2010).

1.6 The aim of the thesis

The aim of the thesis is to show the relationship between the internal and scattered fields, and provide evidence that interference between the partial waves originating from the certain ares in the particle interior are responsible for the non-Rayleigh-like polarization and scattering characteristics for wavelength-scale particles. The studies in Papers I-III show that it is convenient to divide the internal field into two components: the longitudinal component and the transverse component. The longitudinal component is defined as the component parallel to the incident wave vector and the transverse component as the remaining component in the plane perpendicular to the incident wave vector. In Paper IV, the longitudinal component is studied in detail, and it is proposed that focusing of the incident wave is responsible for the localized bright areas in the energy density at the forward part of the particle. It is also shown that these areas are also responsible for the negative polarization at intermediate scattering angles. In Paper V, it is shown that symmetric particles exhibit similar features in the scattered field characteristics at different scattering angles. Simple formulas are used for the size parameter and refractive index to define the angular locations of these features. The physical interpretation explaining the features in the scattered fields is based on the distribution of the internal energy density of the particles. They conclude that the internal field of spherical particles is composed of two main components: a distorted plane wave with apparent wavelength λ/m (m is the relative refractive index) and a standing wave near the particle perimeter with apparent wavelength λ. This standing wave is formed by waves propagating in opposite directions. Due to the circular pattern of the energy density maxima, its relation to the far field can be described as an 'interference dial', which selects destructive/constructive interference at certain scattering angles between the partial waves originating from the maxima.

In Papers VI and VII, the backscattering quantities of hydrometeors are studied at several radar frequencies, and it is shown that the polarization observables, such as the differential reflectivity and the linear depolarization ratio, are very sensitive to particle inhomogeneity and shape. Effective-medium approximations (EMA) cannot be used consistently for these quantities, especially at the higher radar frequencies, when the particles are wavelength-scale. The studies in Paper VI show that the presence of melt water can produce large errors in the computed backscattering quantities, which should be taken into account in modeling. In Paper VII, it is found that, when computations for exact shape models are compared to those for homogeneous spheroids using EMAs, the exact shapes do not show any interference features that are characteristic of spheroids. It is suggested that these differences could be explained by the regular structure of the internal field for spheroids. In the introductory part of the thesis, we make a new case study, which uses the tools developed for Papers IV and V, and apply them to radar backscattering by snowflakes in Paper VII. The suggestion is verified at least for one case.

The thesis is organized as follows. In Sect. 2, the theories of electromagnetic scattering are introduced, and relevant scattering quantities are defined. Section 3 presents various shape models used in the studies. In Sect. 4, the numerical scattering models are introduced, and in Sect. 5, the interference mechanisms for the internal field components are introduced and the results for wavelength-scale particles are summarized. Sect. 6 provides the summaries of the papers in the thesis, while Sect. 7 presents the conclusions of the studies and future prospects. The included papers of the thesis are shown after the introductory part.

2 Theory of electromagnetic scattering

2.1 Basic theory

The macroscopic electromagnetic fields inside matter can be described by the Maxwell equations (Jackson 1998)

$$\begin{aligned}
\nabla \cdot \mathbf{D}(\mathbf{r},t) &= \rho(\mathbf{r},t), \\
\nabla \times \mathbf{E}(\mathbf{r},t) &= -\frac{\partial \mathbf{B}(\mathbf{r},t)}{\partial t}, \\
\nabla \cdot \mathbf{B}(\mathbf{r},t) &= 0, \\
\nabla \times \mathbf{H}(\mathbf{r},t) &= \mathbf{J}(\mathbf{r},t) + \frac{\partial \mathbf{D}(\mathbf{r},t)}{\partial t},
\end{aligned} \tag{1}$$

where $\mathbf{D}$ is the electric displacement, $\mathbf{E}$ the electric field, $\mathbf{B}$ the magnetic induction, $\mathbf{H}$ the magnetic field, ρ the macroscopic charge density, and $\mathbf{J}$ the macroscopic current density. The charge and current densities are related through the continuity equation

$$\frac{\partial \rho(\mathbf{r},t)}{\partial t} + \nabla \cdot \mathbf{J}(\mathbf{r},t) = 0. \tag{2}$$

The field vectors in Eqs. (1) are related through the electromagnetic properties of the (non-dispersive) matter

$$\begin{aligned}
\mathbf{D}(\mathbf{r},t) &= \epsilon(\mathbf{r})\mathbf{E}(\mathbf{r},t), \\
\mathbf{B}(\mathbf{r},t) &= \mu(\mathbf{r})\mathbf{H}(\mathbf{r},t), \\
\mathbf{J}(\mathbf{r},t) &= \sigma(\mathbf{r})\mathbf{E}(\mathbf{r},t),
\end{aligned} \tag{3}$$

where ϵ, μ, and σ are the electric permittivity, magnetic permeability, and conductivity of the matter, respectively.

At the boundary of a particle, the electromagnetic properties can change abruptly, and produce discontinuity for the field vectors. Therefore, it is required that certain conditions are valid at the boundary

$$\begin{aligned}
(\mathbf{B}_2 - \mathbf{B}_1) \cdot \mathbf{n} &= 0, \\
(\mathbf{D}_2 - \mathbf{D}_1) \cdot \mathbf{n} &= \rho_S, \\
\mathbf{n} \times (\mathbf{E}_2 - \mathbf{E}_1) &= \mathbf{0}, \\
\mathbf{n} \times (\mathbf{H}_2 - \mathbf{H}_1) &= \mathbf{J}_S,
\end{aligned} \tag{4}$$

where the subscripts 1 and 2 denote the two media with different properties, $\mathbf{n}$ the surface normal at the boundary, ρ_S the surface charge density, and $\mathbf{J}_S$ the surface current density. In the absence of surface charges and currents, the boundary conditions state that the normal components of $\mathbf{B}$ and $\mathbf{D}$, and the tangential components of $\mathbf{E}$ and $\mathbf{H}$ are continuous across the boundary.

For time-harmonic (oscillating) plane waves propagating in a homogeneous, linear, isotropic, and non-absorbing medium, the electric ($\mathbf{E}$) and magnetic ($\mathbf{H}$) fields are always in phase and oscillating in orthogonal directions with respect to the direction of propagation and each other. The complex-field representation of the waves is

$$\begin{aligned}
\mathbf{E}(\mathbf{r},t) &= \mathbf{E}_0 \exp(\mathrm{i}\mathbf{k} \cdot \mathbf{r} - \mathrm{i}\omega t), \\
\mathbf{H}(\mathbf{r},t) &= \mathbf{H}_0 \exp(\mathrm{i}\mathbf{k} \cdot \mathbf{r} - \mathrm{i}\omega t),
\end{aligned} \tag{5}$$

where $\mathbf{r}$ is the radius vector from an arbitrary origin, $\mathbf{k}$ the wave vector, and ω the angular frequency of the wave.

The Maxwell equations can be combined to produce the electromagnetic wave equations for the time-harmonic fields:

$$\begin{aligned} \nabla^2\mathbf{E} + k^2\mathbf{E} &= 0, \\ \nabla^2\mathbf{H} + k^2\mathbf{H} &= 0, \end{aligned} \tag{6}$$

which are valid for any superposition of time-harmonic plane waves. In addition, the wave vector of the propagating wave must satisfy

$$\mathbf{k} \cdot \mathbf{k} = \omega^2 \epsilon \mu, \tag{7}$$

which can also be expressed in terms of the complex refractive index m,

$$m^2 = \frac{\epsilon\mu}{\epsilon_0\mu_0}, \tag{8}$$

where ϵ_0 and μ_0 are the permittivity and permeability of vacuum, respectively.

The time-averaged energy density of the time-harmonic electromagnetic plane wave in a non-dispersive medium is

$$U(\mathbf{r}) = \frac{1}{2} Re[\epsilon(\mathbf{r})] |\mathbf{E}_0|^2. \tag{9}$$

2.2 Light scattering theory

Light scattering is a common phenomenon happening in all media that contains atoms. A macroscopic particle is composed of a large number of small volume elements, dipoles. When the particle is illuminated by an electromagnetic wave, i.e., an oscillating applied field, it induces a dipole moment into the volume elements and excites the dipoles. The dipoles start to oscillate as a response to the field with the same frequency, and produce secondary radiation. The scattered wave is formed by superposing all the partial waves reradiated by the dipoles. This scattered radiation can be observed in any direction and varies with the physical properties of the particle and the scattering direction. The fraction of the total amount of the scattered energy density in a given direction is described by the phase function of the particle.

There are usually three reference frames that are used in scattering problems: the particle reference frame, the incident wave reference frame, and the scattered wave reference frame. The shape and orientation of the particle are usually defined in the particle reference frame, which can be chosen arbitrarily and independently from the other frames. The incident wave vector and incident polarization of the electromagnetic wave define the incident wave reference frame. The wave vectors of the incident and scattered wave define the scattered wave reference frame. Since the particle reference frame is always bound to the particle and stationary, it is a laboratory reference frame. This is not required for the other frames.

Figure 4 shows the geometry of the scattering from an arbitrary particle as defined by Bohren & Huffman (1983). All scattering quantities are derived in the scattered wave reference frame, usually with respect to the scattering plane, which is determined by the incident and scattering wave vectors, $\mathbf{k}_\mathrm{i} = k_\mathrm{i}\hat{\mathbf{e}}_\mathrm{z}, \mathbf{k}_\mathrm{s} = k_\mathrm{s}\hat{\mathbf{e}}_\mathrm{r}$, respectively ($\hat{\mathbf{e}}_\mathrm{r}$ is the unit vector to the scattering direction). In the far-field region ($kr \gg 1$), the scattered wave, specified by the scattering field vector $\mathbf{E}_\mathrm{s}$, is spherical and transverse: $\hat{\mathbf{e}}_\mathrm{r} \cdot \mathbf{E}_\mathrm{s} \approx 0$. The electric fields of the incident and scattered waves can then be divided into two components:

the component parallel to the scattering plane and the component perpendicular to the scattering plane,

$$\begin{aligned}\mathbf{E}_{\mathrm{i}} &= E_{\|\mathrm{i}}\hat{\mathbf{e}}_{\|\mathrm{i}} + E_{\perp\mathrm{i}}\hat{\mathbf{e}}_{\perp\mathrm{i}}, \\ \mathbf{E}_{\mathrm{s}} &= E_{\|\mathrm{s}}\hat{\mathbf{e}}_{\|\mathrm{s}} + E_{\perp\mathrm{s}}\hat{\mathbf{e}}_{\perp\mathrm{s}}.\end{aligned} \tag{10}$$

The direction of scattering is specified by the scattering angle θ (in the scattering plane) and the azimuth angle ϕ (perpendicular to the scattering plane). In scattering methods, it is usually assumed that the propagation direction of the incident wave coincides with the Z-axis of the particle reference frame.

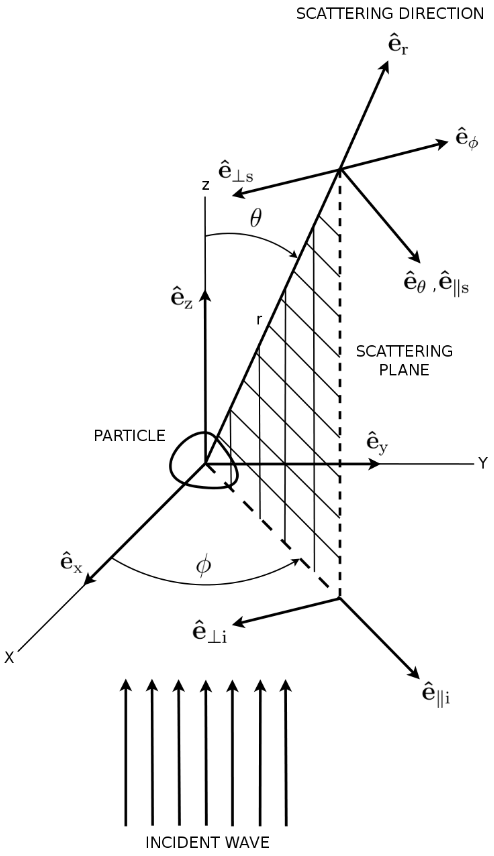

Figure 4: The scattering geometry of an arbitrary particle.

2.3 Stokes vector and Mueller matrix

The polarization state of an electromagnetic wave can be expressed using the Stokes vector $\mathrm{I} = \{I, Q, U, V\}$. The relation between the Stokes vectors of the incident electromagnetic field $\mathrm{I}_{\mathrm{inc}}$ and the scattered field $\mathrm{I}_{\mathrm{sca}}$ is given by the 4×4 scattering matrix $\mathbf{F}(\theta)$ or the Mueller matrix for single particles,

$$\begin{pmatrix} I_{\mathrm{sca}} \\ Q_{\mathrm{sca}} \\ U_{\mathrm{sca}} \\ V_{\mathrm{sca}} \end{pmatrix} = \frac{1}{k^2r^2} \begin{pmatrix} F_{11} & F_{12} & F_{13} & F_{14} \\ F_{21} & F_{22} & F_{23} & F_{24} \\ F_{31} & F_{32} & F_{33} & F_{34} \\ F_{41} & F_{42} & F_{43} & F_{44} \end{pmatrix} \begin{pmatrix} I_{\mathrm{inc}} \\ Q_{\mathrm{inc}} \\ U_{\mathrm{inc}} \\ V_{\mathrm{inc}} \end{pmatrix}. \tag{11}$$

The degree of linear polarization for unpolarized incident light is $P = -Q/I = -F_{21}/F_{11}$, and the degree of circular polarization is $V/I = F_{41}/F_{11}$, where I is the total intensity of the scattered/incident light. The depolarization ratio is $D = 1 - F_{22}/F_{11}$. Only seven of the sixteen elements of the scattering matrix are independent. The dependencies of the elements are described by Hovenier & van der Mee (2000). Usually the scattering volume is composed of particles in various sizes, shapes, orientations, and refractive indices. Therefore, the elements of the scattering matrix are averages over these properties.

The elements of the Stokes vector are related to the electric field components by

$$\begin{aligned} I &= E_{\parallel}E_{\parallel}^{*} + E_{\perp}E_{\perp}^{*}, \\ Q &= E_{\parallel}E_{\parallel}^{*} - E_{\perp}E_{\perp}^{*}, \\ U &= E_{\parallel}E_{\perp}^{*} + E_{\perp}E_{\parallel}^{*}, \\ V &= i(E_{\parallel}E_{\perp}^{*} - E_{\perp}E_{\parallel}^{*}). \end{aligned} \tag{12}$$

2.4 Amplitude scattering matrix

The relationship between the incident and scattered field is given by the 2 × 2 complex amplitude scattering matrix **S** or the Jones matrix for polarized incident field,

$$\begin{pmatrix} E_{\text{sca},\parallel} \\ E_{\text{sca},\perp} \end{pmatrix} = \frac{e^{ik(r-z)}}{-ikr} \begin{pmatrix} S_2 & S_3 \\ S_4 & S_1 \end{pmatrix} \begin{pmatrix} E_{\text{inc},\parallel} \\ E_{\text{inc},\perp} \end{pmatrix}, \tag{13}$$

The information content of Eqs. (11) and (13) is identical. The equations for computing the scattering matrix elements from the amplitude matrix elements are given by, e.g., Bohren & Huffman (1983). The elements of the amplitude scattering matrix are not observable quantities, but complex representations of the transformation between the incident field and the scattered field. The amplitude scattering matrix is defined only for a single particle in a fixed orientation. The elements S_i $(i = 1, 2, 3, 4)$ of the matrix are complex numbers representing the change in amplitude and phase of the incident field

$$\begin{aligned} S_1 &= a_1 e^{i\phi_1}, \\ S_2 &= a_2 e^{i\phi_2} = a_2 e^{i\phi_1} e^{i(\phi_2-\phi_1)}, \\ S_3 &= a_3 e^{i\phi_3} = a_3 e^{i\phi_1} e^{i(\phi_3-\phi_1)}, \\ S_4 &= a_4 e^{i\phi_4} = a_4 e^{i\phi_1} e^{i(\phi_4-\phi_1)}, \end{aligned} \tag{14}$$

where a_i are the amplitudes and ϕ_i the phases of the amplitude matrix elements. Notice that the phases of the other elements are defined with respect to the S_1 element, providing a common phase factor $e^{i\phi_1}$ leaving only seven independent variables. Since the factor represents only a constant phase for all elements, it can be chosen arbitrarily: $\phi_1 = 0$.

In radar applications, the amplitude matrix elements are sometimes needed for the modeled particles, but these are not always provided by the scattering methods, which usually output only the scattering matrix elements (Eq. 11). If the polarization state of the incident wave is defined using the Stokes vector, the amplitude matrix elements can be obtained from the corresponding scattering matrix elements

$$\begin{aligned} S_1 &= a_1 = [\frac{1}{2}(F_{11} - F_{12} - F_{21} + F_{22})]^{1/2}, \\ S_2 &= a_2 e^{i\phi_2} = \frac{1}{2a_1}[F_{33} + F_{44} + \mathrm{i}(F_{34} - F_{43})], \\ S_3 &= a_3 e^{i\phi_3} = \frac{1}{2a_1}[F_{31} - F_{32} + \mathrm{i}(F_{42} - F_{41})], \\ S_4 &= a_4 e^{i\phi_4} = \frac{1}{2a_1}[F_{13} - F_{23} + \mathrm{i}(F_{14} - F_{24})]. \end{aligned} \tag{15}$$

Notice that there are several ways to formulate Eqs. (15), because only seven from the sixteen elements of the scattering matrix elements are independent. Also notice that Eqs. (15) only hold in fixed orientation. Both **F** and **S** are usually defined in the forward-scattering alignment (FSA) convention in light scattering applications (Ulaby & Elachi 1990). In radar applications, the backscattering alignment (BSA) convention is used. The difference between the conventions is that in FSA the scattering is defined from the viewpoint of the electromagnetic wave, whereas in BSA it is defined from the viewpoint of the transmitter (radar). Mathematically, these are related by

$$\mathbf{S}_{BSA} = \begin{pmatrix} 1 & 0 \\ 0 & -1 \end{pmatrix} \mathbf{S}_{FSA}. \tag{16}$$

2.5 Indirect and direct problems

In inverse/indirect problems, the physical properties of the scatterer are unknown. When the scattered intensities are observed in different polarization states and wavelengths, they reveal the nature by which the electromagnetic field is interacting with the scatterer. This allows to determine and constrain the properties of the scatterer by constructing empirical laws that combine the observed properties to the physical ones.

In direct problems, the physical properties of the scatterer are known or at least assumed to be known. In this case, the scattering can be modeled using a method suitable for the task (see Section 4). The incident field is also assumed to be known. In passive remote sensing, it is usually the sunlight, while for active remote sensing, the transmitted radar/lidar signal. The objective is to compute the unknown scattered intensities. To get results that mimic reality, a set of different sample particles with varying sizes, shapes, refractive indices, and orientations usually need to be created and modeled. The results are averaged over these samples.

In practice, the inverse and direct problems are solved together. The observations of light scattering help to constrain the physical properties that are put into the direct problem. However, this is usually very difficult to achieve mainly due to many sources of uncertainties in the observations. Therefore, direct *in-situ* measurements of the particles themselves can be very helpful to narrow down the physical properties. This is feasible for ground-based applications, such as snowfall measurement, but very difficult for regolith studies of other Solar system bodies. One can thus use terrestrial applications also to test methods intended for astronomical targets. Regolith analog particles can be used as a substitute in this case.

2.6 Radar observables

Polarimetric weather radars transmit short electromagnetic pulses that are polarized in orthogonal incident directions, horizontal (h) and vertical (v), which refer to the local geodetic coordinates of the radar system. In this reference frame, the amplitude scattering matrix in Eq. (13) can be defined using the BSA convention as

$$\begin{pmatrix} E_{\mathrm{sca,v}} \\ E_{\mathrm{sca,h}} \end{pmatrix} = \frac{e^{ik(r-z)}}{-ikr} \begin{pmatrix} S_{\mathrm{vv}} & S_{\mathrm{vh}} \\ S_{\mathrm{hv}} & S_{\mathrm{hh}} \end{pmatrix} \begin{pmatrix} E_{\mathrm{inc,v}} \\ E_{\mathrm{inc,h}} \end{pmatrix}, \tag{17}$$

where $|S_{\mathrm{vh}}|^2 = |S_{\mathrm{hv}}|^2$ due to the reciprocity at backscattering.

The received signal for the different transmitted/received polarizations from a single particle is proportional to its cross section,

$$\begin{aligned}\sigma_{\mathrm{hh}} &= \frac{4\pi}{k^2}|S_{\mathrm{hh}}|^2 = \frac{2\pi}{k^2}(F_{11} - F_{12} - F_{21} + F_{22}) \qquad [\mathrm{m}^2],\\ \sigma_{\mathrm{vv}} &= \frac{4\pi}{k^2}|S_{\mathrm{vv}}|^2 = \frac{2\pi}{k^2}(F_{11} + F_{12} + F_{21} + F_{22}) \qquad [\mathrm{m}^2],\\ \sigma_{\mathrm{vh}} &= \frac{4\pi}{k^2}|S_{\mathrm{vh}}|^2 = \frac{2\pi}{k^2}(F_{11} - F_{12} + F_{21} - F_{22}) \qquad [\mathrm{m}^2], \end{aligned} \tag{18}$$

where F denotes the elements of the scattering matrix (Eq. 11).

In real situations, the scattering medium is composed of many particles with different sizes, shapes, melting phases, and orientations. In this case, the backscattered signal is proportional to the sum of the average scattered intensity from all the particles in the volume observed (averaging is denoted by brackets $\langle\rangle$ hereafter). Several radar observables can be defined based on the total scattering of the medium. The attenuation of the radar signal due to absorption and scattering is usually handled separately and is not included in the definitions.

The horizontal reflectivity

$$Z_{\mathrm{h}} = Cn_0\langle\sigma_{\mathrm{hh}}\rangle, \qquad [\mathrm{mm}^6\ \mathrm{m}^{-3}] \tag{19}$$

where n_0 is the number density of the particles, is the total horizontal reflectivity in a volume for a horizontally polarized incident wave. The coefficient $C = 1.6\times10^{19}/(\pi k^4|K|^2)$ ($|K|^2 = |(\epsilon - \epsilon_0)/(\epsilon + 2\epsilon_0)|^2$ is due to the reflectivity factor of Rayleigh scatterers, when expressed in units of $\mathrm{mm}^6\ \mathrm{m}^{-3}$. Together with other radar observables, Z_{h} is important in identifying different hydrometeor types (e.g., Straka et al. 2000, Liu & Chandrasekar 2000).

The differential reflectivity

$$Z_{\mathrm{DR}} = \frac{\langle\sigma_{\mathrm{hh}}\rangle}{\langle\sigma_{\mathrm{vv}}\rangle} \tag{20}$$

describes the ratio of the backscattered power for horizontally and vertically polarized radar beam, and for particles small compared to the wavelength, is a measure of the reflectivity-weighted mean axis ratio of hydrometeors in a volume.

The linear depolarization ratio

$$\mathrm{LDR}_{\mathrm{vh}} = \frac{\langle\sigma_{\mathrm{vh}}\rangle}{\langle\sigma_{\mathrm{hh}}\rangle} \tag{21}$$

describes the ratio of the backscattered power for horizontally polarized transmitted radar beam received in the vertically polarized channel and the corresponding beam received in the horizontally polarized channel. It is a function of hydrometeor asphericity, thermodynamic phase, and orientation in the plane of polarization. Both Z_{DR} and $\mathrm{LDR}_{\mathrm{vh}}$ are affected by polarization-state-dependent attenuation in the atmosphere. Z_{h}, Z_{DR}, and $\mathrm{LDR}_{\mathrm{vh}}$ are usually expressed as 10log(.) in dB units.

The copolarized correlation coefficient defines two radar observables,

$$\begin{aligned}\rho_{\mathrm{hv}}\exp(\mathrm{i}\delta_{\mathrm{hv}}) &= \frac{\langle S_{\mathrm{hh}}S^*_{\mathrm{vv}}\rangle}{[\langle|S_{\mathrm{hh}}|^2\rangle\langle|S_{\mathrm{vv}}|^2\rangle]^{1/2}},\\ \rho_{\mathrm{hv}} &= \frac{[\langle F_{33} + F_{44}\rangle^2 + \langle F_{43} - F_{34}\rangle^2]^{1/2}}{[\langle F_{11} - F_{12} - F_{21} + F_{22}\rangle\langle F_{11} + F_{12} + F_{21} + F_{22}\rangle]^{1/2}}, \qquad (22)\\ \delta_{\mathrm{hv}} &= \arg(\langle S_{\mathrm{hh}}S^*_{\mathrm{vv}}\rangle) = \arctan\left[\frac{\langle F_{43} - F_{34}\rangle}{\langle F_{33} + F_{44}\rangle}\right], \qquad (23)\end{aligned}$$

where ρ_{hv} is the amplitude and δ_{hv} the argument of the correlation coefficient. ρ_{hv} is a measure of the degree of correlation between the horizontally and vertically polarized backscattered waves. It measures the variability in the horizontal and vertical sizes of hydrometeors and is sensitive to mixtures of particles with different phases. δ_{hv} is a measure of non-Rayleigh-like scattering by partially aligned scatterers. Neither ρ_{hv} nor δ_{hv} are affected by attenuation. δ_{hv} is also known as the backscatter differential phase.

The specific differential phase

$$K_{\mathrm{DP}} = 10^3(\frac{180}{\pi})(\frac{2\pi}{k})n_0 Re[\langle S_1(\mathbf{k},\mathbf{k}) - S_2(\mathbf{k},\mathbf{k})\rangle] \qquad [\mathrm{deg\ km}^{-1}] \tag{24}$$

is the difference between the propagation constants for horizontally and vertically polarized waves, and can be used to measure the difference in attenuation for the horizontal and vertical signals. It is also used to distinquish between statistically isotropic and anisotopic hydrometeors.

It should be noted that multiple scattering between the particles is not included in the definitions. According to Battaglia et al. (2005), its contribution to the signal is negligible when compared to single scattering. It is usually assumed that the number densities are small enough that near-field effects between the particles can also be neglected.

3 Shape models

There are no perfect shapes in nature. Due to the chaotic and stochastic behavior of natural phenomena, there is a variation of shapes in both macroscopic and microscopic scales from idealized shape models. As shape is one of the most important physical property of particles in scattering, it is therefore crucial to try to model it as realistically as possible. Due to the large variation in real shapes, it is usually not important to be deterministic in the modeling. Stochastic similarity is usually sufficient in order to obtain the relevant scattering quantities for the study. This is the main principle used in the thesis.

3.1 Simple models

Regularity and symmetry in shape has its advantages when modeling scattering. For simple shapes, such as spheres, cubes, cylinders, and spheroids, it is possible to solve the scattering exactly/analytically. This means that, as long as the implementation is convergent, one can be confident that the accuracy of the results is sufficient regardless of the other physical properties of the particle. Simple shape models can also be used as a comparison to check accuracy of approximate scattering models, and to demonstrate the effect of irregularity on the scattering quantities. However, due to the availability of computer resources and improved models, it is no longer necessary to restrict solely to simple shapes. Simple shape models have been used in Papers I, II, IV, V, VI, and, VII.

3.2 Gaussian-random-sphere model

Gaussian-random-sphere particles (GRS) are nonspherical particles with a random variation in the radius obeying multivariate lognormal statistics (Muinonen et al. 1996). The size is specified by the mean radial distance a. The radius vector of a Gaussian-random sphere particle is

$$\begin{aligned} r(\theta,\phi)\mathbf{e}_r &= \frac{a\exp\left(s(\theta,\phi)\right)}{\sqrt{1+\sigma^2}}\ \mathbf{e}_r, \\ s(\theta,\phi) &= \sum_{l=0}^{\infty}\sum_{m=-l}^{l} s_{lm}\,Y_{lm}(\theta,\phi), \end{aligned} \tag{25}$$

where σ is the relative standard deviation of radial distance, $s = s(\theta,\phi)$ is the logarithmic radial distance, Y_{lm} are the orthonormal spherical harmonics, and s_{lm} are Gaussian random variables with zero means.

If the angular separation between two directions (θ_1,ϕ_1) and (θ_2,ϕ_2) is denoted by ϑ, the covariance function $\Sigma_s(\vartheta)$ describes the autocovariance between two random variables $s(\theta_1,\phi_1)$ and $s(\theta_2,\phi_2)$. It can be expressed as a series of Legendre polynomials

$$\Sigma_s(\vartheta) = \sum_{l=0}^{l_{\max}} C_l P_l(\cos\vartheta), \tag{26}$$

where the coefficients $C_l \geq 0$, and the series in truncated to some finite value denoted by $l_{\max}$. The coefficients can be defined as a power-law function

$$\sum_{l=0}^{l_{\max}} C_l = C\sum_{l=0}^{l_{\max}} l^{-\nu} = \ln(1+\sigma^2), \tag{27}$$

where C is a normalization constant, and ν the power-law index of the covariance function. In this case, the covariance function is governed by σ and ν.

The GRS model has been used to study asteroid shapes (Muinonen 1998), Solar system dust particles (Muinonen 1996, Muinonen et al. 2007), ice particles (Nousiainen & McFarquhar 2004), and dust particles in the Earth's atmosphere (Veihelmann et al. 2006, Nousiainen, Muñoz, Lindqvist, Mauno & Videen 2011). One of the justifications for applying the GRS model to these particles is the central limit theorem, which states that the shape parameters of natural particles, with finite mean and variance, exhibit normal statistics for large numbers of random samples. The GRS model was used in Papers II, III, and V. A sample shape with $\sigma = 0.245$ and $\nu = 4$ is shown in Fig. 5 (left).

3.3 Agglomerated-debris model

Since natural particles exhibit surface roughness in all length scales, it is useful to use a shape model that incorporates rough structure. Zubko et al. (2007) showed that, when introducing roughness to the GRS model, the degree of linear polarization is very sensitive to this, and generally increased at intermediate scattering angles as roughness increased. Near the backscattering direction, increasing roughness resulted in a non-monotonic behavior with respect to the refractive index and the size parameter.

Zubko et al. (2005) introduced the agglomerated-debris model (AD) for interplanetary dust particles. They are generated from a spherical particle by damaging it in a random way. The spherical particle is projected initially upon a three-dimensional lattice of dipoles. This lattice is divided into two parts: the surface layer and the internal region. Among the surface dipoles, about 0.8% are chosen randomly to be seed particles of empty space. Among the internal dipoles, about 0.016% are chosen randomly to be seed particles having the refractive material of the irregular particle, and about 0.016% are chosen randomly to be seed particles of empty space. After this initial random selection, all the other dipoles within the lattice are marked as having the optical properties of empty space or of the material, based on which type of seed dipole lies closest. The resulting particle resembles highly irregular agglomerated debris. The material in these particles occupies only about 26% of the volume, which makes them rather fluffy. The AD model is also used in Paper IV. A sample shape of an AD particle is shown in Fig. 5 (right).

3.4 Fractal model

In addition to irregularity and roughness, some natural particles also exhibit fractal structure, i.e., self-similarity in finite length scales. Typical examples are soot particles (Samson et al. 1987), snowflakes (Schmitt & Heymsfield 2010) and dendritic ice crystals in the Earth's atmosphere (Shibkov et al. 2003).

In Paper VII, we use the fractal model by Ishimoto (2008). In the model, the snowflake is generated by an iterative procedure in a cubic lattice, starting with a single ice element at the center of the lattice. At each iteration step, the lattice size is doubled in each dimension, and a number of new ice elements are positioned at random lattice sites adjacent to the existing elements. The total number of elements occupied after each iteration step is controlled by the fractal dimension fd

$$N_i = 2^{\mathrm{i}(fd+0.2)}, i = 1, ..., N_{\mathrm{iter}}, \tag{28}$$

where the additional factor 0.2 is introduced in order to preserve the box dimensions of the fractals.

Due to the lattice representation of the fractal, it is straightforward to convert the generated shapes for the discrete-dipole approximation (Sect. 4.5). There are a few disadvantages of using the fractal model to represent real snowflakes. One is that, especially

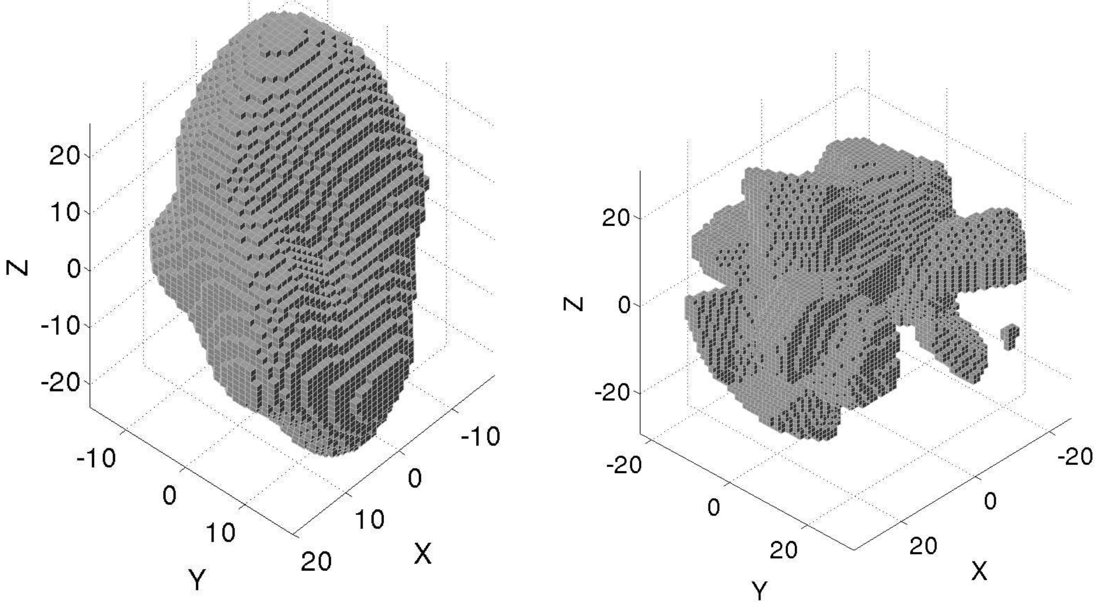

Figure 5: Examples of a Gaussian-random-sphere (left) and an agglomerated debris particle (right).

for small fractal dimension ($fd < 2.0$), some parts of the fractal can be separated and would not be snow aggregates in a strict sense. Another disadvantage is that, in order to model very large snowflakes, the number of maximum iterations must be so large ($N_{\text{iter}} > 8$) that the available computer memory will become a limiting factor. This can be circumvented to some degree by increasing the lattice spacing. Sample shapes of fractal particles are shown in Fig. 6.

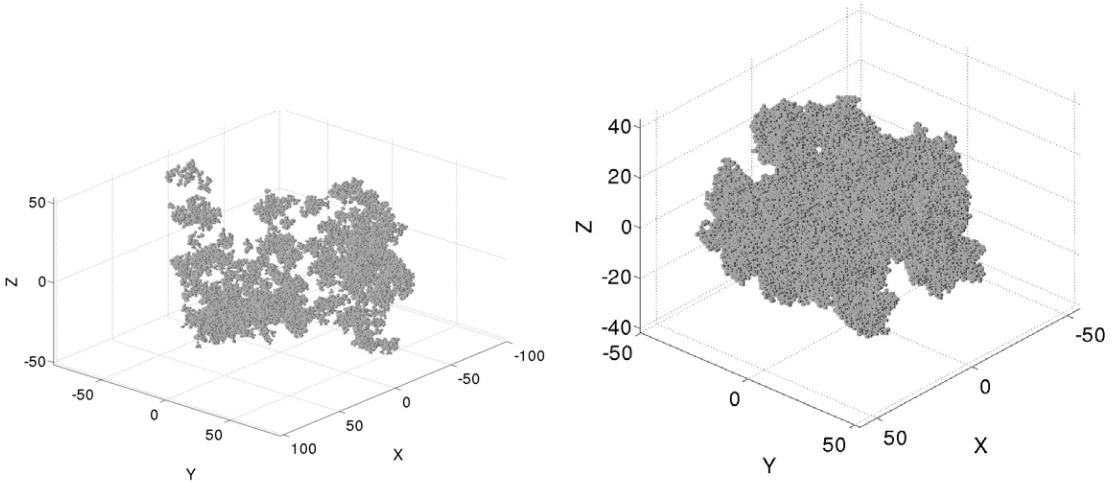

Figure 6: Examples of fractal particles with the fractal dimension $fd = 1.88$ (left) and $fd = 2.4$ (right). Number of iterations $N_{\text{iter}} = 7$.

3.5 Aggregation model for ice crystals

Compared to the mathematical model of fractal particles, a more physical way to represent snowflakes is a model that simulates the aggregation process of ice crystals. In Paper VII, the model by Westbrook (2004) is implemented. The model simulates the aggregation process in a physically realistic way using an iterative and stochastic approach. First, a cloud of single ice crystals in random orientations is generated. During each iteration step, two aggregates or single ice crystals, specified by indices i and j, are chosen randomly from the generated cloud and placed in random positions within the cross sections defined by their radii of gyration

$$R_{\mathrm{gyr,i}} = \left[\frac{\sum_{l=1}^{N_i} r_l^2 m_l}{\sum_{l=1}^{N_i} m_l} \right]^{1/2}, \tag{29}$$

where m_l is the mass and r_l the radial distance of the lth dipole from the center of mass, and N_i the number of dipoles in aggregate i. For two aggregates with maximum radii $R_{\mathrm{max,i}}$, $R_{\mathrm{max,j}}$, and falling speeds v_i, v_j, the probability of collision

$$\Gamma_{ij} \propto \pi (R_{\mathrm{max,i}} + R_{\mathrm{max,j}})^2 |v_i - v_j|. \tag{30}$$

If there is a collision, the particles are connected from their nearest points projected to the horizontal plane. The generated aggregate is returned to the cloud. If there is no collision, a new pair is chosen randomly.

In our model, we reorient the new aggregates based on their maximum moment of inertia. This increases their radii of gyration, which are computed with respect to the vertical axis. According to, e.g., Cho et al. (1981), ice crystals tend to fall with their major dimensions oriented horizontally. One advantage of the aggregation model is that the single ice crystals can be generated beforehand with other algorithms and then rescaled and reoriented according to known relationships between the physical properties of crystals and different habits. One disadvantage is that the model does not take into account snowflake break-up during aggregation. This might make the generated particles fluffier than real snowflakes. Sample shapes of aggregate particles are shown in Fig. 7.

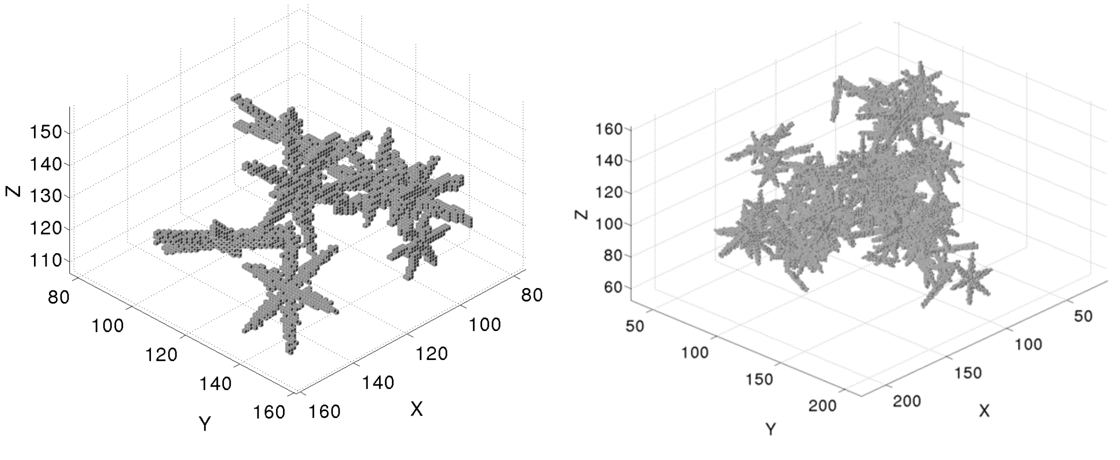

Figure 7: Examples of aggregate particles with ten (left) and one hundred dendritic ice crystals (right).

4 Scattering methods

For particles smaller than the wavelength, i.e., in the Rayleigh region, the applied field of the particle can be considered to be homogeneous and therefore does not produce shape-dependent effects in scattering. However, the varying dimensions of the particle respond to the incident field differently, especially for particles in fixed or preferential orientations. These differences can be seen in the polarimetric quantities. For particles comparable in size to the wavelength, i.e., wavelength-scale particles, the applied field is no longer homogeneous and various interference phenomena can produce distinct features in the scattered field, which vary as a function of size, shape, refractive index, and orientation of the particle.

4.1 Rayleigh approximation

When the size of the scatterer, specified by the size parameter, is small compared to the wavelength, the applied field $\mathbf{E}_0$, incident on the scatterer, can be approximated to be homogeneous inside the particle and the particle can be approximated as a single dipole. The applied field induces a dipole moment

$$\mathbf{P} = \beta \mathbf{E}_0 \tag{31}$$

in the particle, where β is the polarizability tensor of the particle. This is called the electrostatics approximation. The conditions for the approximation are: $x \ll 1$ (small size relative to the external wavelength) and $|m|x \ll 1$ (small size relative to the internal wavelength). If the particle is spherical and composed of isotropic matter, β is scalar and isotropic, i.e., its polarimetric properties do not depend on the propagation direction or how the applied field is polarized. However, if the particle is nonspherical, β is no longer scalar. For example, if the particle is ellipsoidal with dimensions (a,b,c) in Cartesian coordinates, the polarizability tensor

$$\beta = V \begin{pmatrix} \frac{m^2-1}{1+L_1(m^2-1)} & 0 & 0 \\ 0 & \frac{m^2-1}{1+L_2(m^2-1)} & 0 \\ 0 & 0 & \frac{m^2-1}{1+L_3(m^2-1)} \end{pmatrix}, \tag{32}$$

where $V = 4\pi abc/3$ is the volume of the ellipsoid, and L_i ($L_1 + L_2 + L_3 = 1$) are the geometric factors, which are one-dimensional integrals. For oblate spheroids (e.g., van de Hulst 1957),

$$L_3 = \frac{1+f^2}{f^2}(1 - \frac{\arctan f}{f}), \tag{33}$$

where $f^2 = a^2/c^2 - 1$, and $L_1 = L_2$. Here the polarizability is a diagonal tensor, because the incident wave reference frame coincides with the principal axes of the ellipsoid. For other incident wave or particle reference frames, as described by Gledhill & McCall (2000) and Battaglia et al. (1999), the polarizability tensor of the spheroid can be obtained by rotating the coordinate system with two Euler rotations specified by the angles (α_E,β_E)

$$\beta' = \mathbf{T}^{-1}\beta\mathbf{T}, \tag{34}$$

where the rotation matrix

$$\mathbf{T} = \begin{pmatrix} \cos\alpha_E \cos\beta_E & \sin\alpha_E \cos\beta_E & -\sin\beta_E \\ -\sin\alpha_E & \cos\alpha_E & 0 \\ \cos\alpha_E \sin\beta_E & \sin\alpha_E \sin\beta_E & \cos\beta_E \end{pmatrix}. \tag{35}$$

In a time-harmonic applied field, the dipole oscillates with the same period as the applied field with the amplitude specified by the induced dipole moment. The elements of the amplitude scattering matrix are given by

$$\begin{aligned}
S_1 &= \mathrm{i}k^3 \sum_{k=1}^{3} T_{k2}\beta_k T_{k2}, \\
S_2 &= \mathrm{i}k^3 (\cos\theta \sum_{k=1}^{3} T_{k1}\beta_k T_{k1} - \sin\theta \sum_{k=1}^{3} T_{k3}\beta_k T_{k1}), \\
S_3 &= \mathrm{i}k^3 (\cos\theta \sum_{k=1}^{3} T_{k1}\beta_k T_{k2} - \sin\theta \sum_{k=1}^{3} T_{k3}\beta_k T_{k2}), \\
S_4 &= \mathrm{i}k^3 \sum_{k=1}^{3} T_{k2}\beta_k T_{k1}, \qquad (36)
\end{aligned}$$

which for a spherical particle reduces to $S_1 = \mathrm{i}k^3\beta$, $S_2 = \mathrm{i}k^3\beta\cos\theta$, $S_3 = 0,$, and $S_4 = 0$.

For Rayleigh-type scattering, the degree of linear polarization for unpolarized incident light is a bell-shaped curve with a maximum at the exact 90° scattering angle (Fig. 8; right panel). As can be seen, the positive polarization peak is due to the perpendicular component of the scattered field dominating over the parallel component at intermediate scattering angles (Fig. 8; left panel).

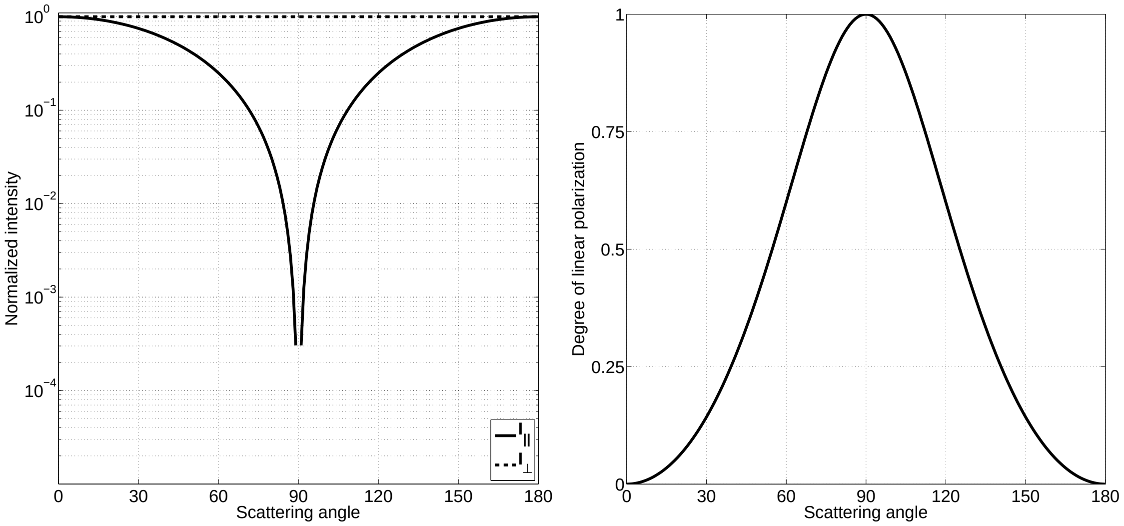

Figure 8: The parallel and perpendicular intensities (left panel, solid and dotted lines, respectively) and the degree of linear polarization (right panel) for a small sphere ($x = 0.001$).

4.2 Lorenz-Mie theory

The interaction of an electromagnetic plane wave with a spherical particle in a non-absorbing medium was first described independently by four authors: Lorenz (1890), Love (1899), Mie (1908) and Debye (1909). When the wave equations (Eq. 6) are solved in spherical polar coordinates, the electromagnetic field can be described by the vector spherical wave functions **M** and **N** as (e.g., Bohren & Huffman 1983)

$$\begin{aligned}\mathbf{E}_{\text{inc}} &= \sum_{n=1}^{\infty}\sum_{m=-n}^{n}(a_{mn}\mathrm{Rg}\mathbf{M}_{mn} + b_{mn}\mathrm{Rg}\mathbf{N}_{mn}),\\ \mathbf{E}_{\text{int}} &= \sum_{n=1}^{\infty}\sum_{m=-n}^{n}(c_{mn}\mathrm{Rg}\mathbf{M}_{mn} + d_{mn}\mathrm{Rg}\mathbf{N}_{mn}),\\ \mathbf{E}_{\text{sca}} &= \sum_{n=1}^{\infty}\sum_{m=-n}^{n}(p_{mn}\mathbf{M}_{mn} + q_{mn}\mathbf{N}_{mn}),\end{aligned} \tag{37}$$

where (a,b) are the coefficients for the incident electric field, (c,d) the coefficients for the internal electric field, and (p,q) the coefficients for the scattered electric field. Rg denotes the fact that the spherical Bessel functions must be regular at the origin for both the incident and internal fields. The coefficients are functions of the size parameter and the refractive index of the sphere, and can be determined from the boundary conditions between the scatterer and the medium. Notice that the incident wave expansion requires regularity at the origin. Also, the scattered wave expansion has been shown to be valid outside the circumscribing sphere of the particle.

In practical implementations, the infinite series in Eqs. (37) are usually truncated to certain N *a priori*. This is due to the limited precision of the floating-point arithmetic, when performing upward recurrence for the coefficients (Bessel functions). According to Wiscombe (1980), a sufficient criterion to guarantee convergence is an integer closest to

$$N = \begin{cases} x + 4x^{1/3} + 1 & 0.02 \le x \le 8 \\ x + 4.05x^{1/3} + 2 & 8 < x < 4200 \\ x + 4x^{1/3} + 2 & 4200 \le x \le 20000, \end{cases} \tag{38}$$

where the $x^{1/3}$-terms have been added in order to include edge wave contributions that exhibit resonance effects (e.g., Pluchino 1981). Generally, for $n < x$, the asymptotic behavior of the Bessel functions is oscillatory, whereas for $n > x$, it is exponentially decreasing. This behavior is explained by van de Hulst (1957) based on the localization principle. It states that a term of the order n corresponds to a ray passing the origin at a distance $(n+\frac{1}{2})\lambda/2\pi$. Rays hitting the sphere correspond to $n+\frac{1}{2} < x$, and rays passing the sphere correspond to $n+\frac{1}{2} > x$.

The relation of the internal field and scattered field in resonance modes for large spherical particles has been studied by, e.g., Fahlen & Bryant (1968), Chylék et al. (1980), Probert-Jones (1984), and Chylék et al. (1985). According to Chylék et al. (1980), the ripple structure in extinction and sharp spikes in the backscattering are due to resonances in the partial wave scattering amplitudes. They also show that by removing a particular n-mode from the Mie solution, one spike will disappear from the scattered field. Probert-Jones (1984) shows, using the localization principle, that the sharp spikes in the backscattering at certain size parameters cannot be attributed to surface waves/rays, but that each spike originates from a certain coefficient a_n and b_n. At least for large spheres, these resonance modes correspond to an increase in internal energy density at $r/a \sim 1/m$ (a is the radius, and r the radial distance from the center). Near the surface they form a spherical standing wave.

Due to the symmetry of spherical particles, there is no cross-polarization terms in the amplitude scattering matrix (S_3=S_4=0), and therefore no depolarization of the incident field. Because of this, only three of the elements in the scattering matrix are independent: $F_{11}^2 = F_{12}^2 + F_{33}^2 + F_{34}^2$. Also, wavelength-scale spherical particles exhibit a wide range of values for the degree of linear polarization, as can be seen in Fig. 9.

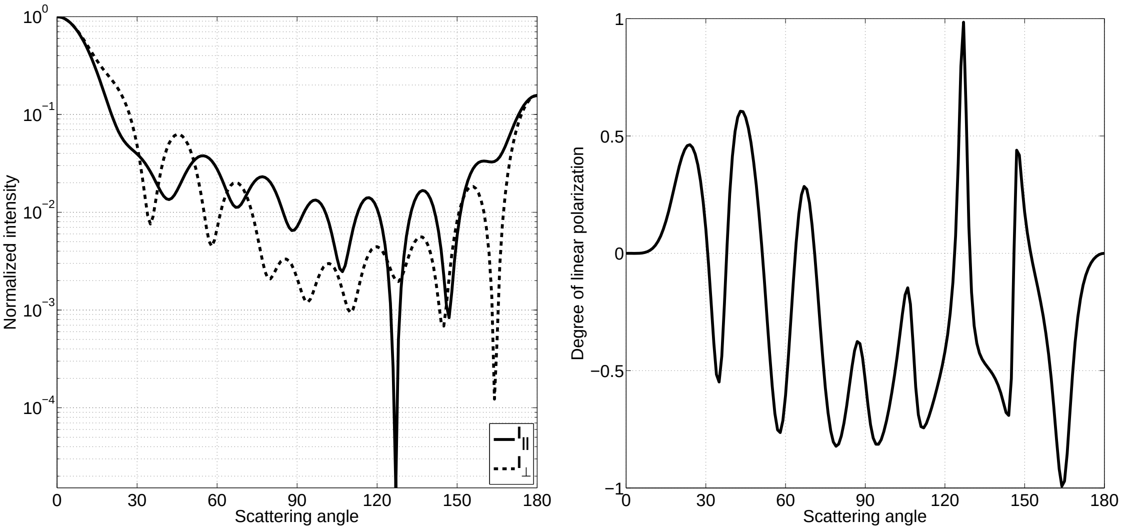

Figure 9: Same as in Fig. 8, but for a sphere with size parameter $x = 8$ and refractive index $m = 1.55$.

The Lorenz-Mie theory has been extended for concentrically layered spheres by Aden & Kerker (1951) and aggregates of spheres by Bruning & Lo (1971).

4.3 *T*-matrix method

The T-matrix method (TMM) is an exact method for computing scattering from wavelength-scale, homogeneous, and nonspherical particles. It was initially based on the extended boundary condition method by Waterman (1965), who applied it to single homogeneous particles. Peterson & Ström (1973) extended it to multilayered particles and clusters of nonspherical particles. Although TMM is applicable to any star-like particle (i.e., a particle which has a single-valued radial distance for each surface point), in practice the shapes that can be modeled with TMM are usually spheroids, finite circular cylinders, Chebyshev particles (Mishchenko 2000), and polyhedra (Kahnert et al. 2001). This is mainly because symmetries in particle shape can be utilized in TMM resulting in significant improvement in execution times. For general non-axisymmetric particles, there are a few methods available (Wriedt & Doicu 1997, Laitinen & Lumme 1998, Petrov et al. 2011).

TMM expands the incident, internal, and scattered fields as vector spherical wave functions. It computes the T matrix, which transforms the incident field coefficients to the scattered field coefficients. With the boundary conditions for the incident and internal fields, the coefficients for the internal field can be determined with the matrix $\mathbf{Q}$

$$\begin{pmatrix} \mathbf{a}_{inc} \\ \mathbf{b}_{inc} \end{pmatrix} = \begin{pmatrix} \mathbf{Q}_{11} & \mathbf{Q}_{12} \\ \mathbf{Q}_{21} & \mathbf{Q}_{22} \end{pmatrix} \begin{pmatrix} \mathbf{c}_{int} \\ \mathbf{d}_{int} \end{pmatrix}, \tag{39}$$

where the elements of $\mathbf{Q}$ are surface integrals that depend on the shape, size, and refractive index of the particle. Using the boundary conditions again for the internal and scattered fields, the coefficients for the scattered field are found with the matrix Rg$\mathbf{Q}$

$$\begin{pmatrix} \mathbf{p}_{sca} \\ \mathbf{q}_{sca} \end{pmatrix} = -\begin{pmatrix} \mathrm{Rg}\mathbf{Q}_{11} & \mathrm{Rg}\mathbf{Q}_{12} \\ \mathrm{Rg}\mathbf{Q}_{21} & \mathrm{Rg}\mathbf{Q}_{22} \end{pmatrix} \begin{pmatrix} \mathbf{c}_{int} \\ \mathbf{d}_{int} \end{pmatrix}, \tag{40}$$

where the elements of Rg$\mathbf{Q}$ are also surface integrals similar to the matrix $\mathbf{Q}$. Using Eqs.

(39) and (40), the T matrix of the particle can be found,

$$\mathbf{T} = -\mathrm{Rg}\mathbf{Q}\mathbf{Q}^{-1}, \tag{41}$$

and it can be used to compute any scattering quantity for a given incident field. The validity of TMM near the particle surface is uncertain and depends on the shape of the particle. According to the Rayleigh hypothesis, the scattered field expansion is valid near the surface, but its applicability to rough surfaces was criticized by, e.g., Lippmann (1953). More recent investigations have also shown that there can be convergence issues with TMM, when a spheroidal particle is close to a plane interface indicating that the hypothesis may not be valid in this case (Doicu et al. 1999).

One advantage of TMM is that the T matrix needs only to be computed once for a given particle shape, size, orientation, and refractive index. The scattering problem can then be solved for any incident and scattered direction or polarization. This is a distinct advantage of TMM against volume-integral methods, such as the discrete-dipole approximation (DDA). The disadvantage is that TMM is applicable to homogeneous particles only. TMM has been further developed into the null-field method with discrete sources (NFM-DS), reviewed by Wriedt (2007). NFM-DS has less restrictions on shape, and can even be applied to inhomogeneous particles (Schmidt & Wriedt 2009).

4.4 Effective-medium approximation

Particle inhomogeneity can be accounted for with the effective-medium approximation (EMA) by replacing the inhomogeneous particle with an equivalent homogeneous particle. When the exact composition of a particle is not known or the scattering must be computed relatively fast, it is usually practical to average the optical properties of a composite particle, e.g., by using EMA. There are many EMAs available (Chýlek et al. 2000), with the Maxwell-Garnett (M-G) and the Bruggeman formulas being the most common. Sihvola (1989) provides a generic mixing formula that includes both the M-G and Bruggeman formulas. It is usually assumed that one constituent is the matrix, and the other constituents are the inclusions that are embedded in the matrix. The inclusions are assumed to be spherical or ellipsoidal, uniformly distributed, and must be much smaller than the wavelength. In M-G, the effective relative permittivity

$$\epsilon_{\mathrm{eff}} = \epsilon_m \frac{\epsilon_i(1+2f_i) + \epsilon_m(1+2f_m)}{\epsilon_i(1-f_i) + \epsilon_m(3-f_m)}, \tag{42}$$

where f_i and f_m, $f_i + f_m = 1$, are the volume fractions of the inclusion and the matrix, respectively, and ϵ_i and ϵ_m are the relative permittivies. Notice that Eq. (42) produces a different value for ϵ_{eff} when switching between the inclusion and the matrix. Eq. (42) can also be generalized to have multiple asymmetric inclusions. For a three component case, Eq. (42) can be applied twice. First, two of the three components are mixed, and then the resulting effective medium is mixed with the remaining constituent. This results in six possible combinations. Fabry & Szyrmer (1999) and Russchenberg & Ligthart (1996) investigated which combinations produce best estimate for the radar reflectivity, when used in a melting-layer model and compared to observations. Meneghini & Liao (2000) provided an extended EMA that is derived from the average internal field amplitudes of the scattering elements. Applicability of EMAs to model snowflakes was studied in Papers VI and VII.

4.5 Discrete-dipole approximation

The discrete-dipole approximation is a numerical method commonly used to compute light scattering by irregularly shaped particles. It was first introduced by DeVoe (1964) for small aggregate particles. The currently adopted theory, however, is based on the coupled dipole method by Purcell & Pennypacker (1973), in which the particle is discretized as a set of dipoles on a cubic lattice. The dipoles are separated by a dimensionless distance kd. Each dipole has the optical response of the material located in the corresponding real space. This is represented by the dipole moment $\mathbf{P}_i$ for the ith dipole. Once $\mathbf{P}_i$ has been computed for each dipole, any scattering quantity can be obtained by using the volume-integral equation. Mathematically, $\mathbf{P}_i$ $(i = 1, 2, ..., N)$ are found from a linear system of equations

$$\mathbf{E}_i^{\mathrm{inc}} = \beta_i^{-1}\mathbf{P}_i + \sum_{j\neq i}\mathbf{G}(\mathbf{r}_i, \mathbf{r}_j)\mathbf{P}_j, j = 1, 2, ..., N, \tag{43}$$

where $\mathbf{E}_i^{\mathrm{inc}} = \mathbf{E}_0 e^{\mathrm{i}\mathbf{k}\cdot\mathbf{r}_i}$ is the incident field at dipole i, $\mathbf{P}_i$ the dipole moment at dipole i, β_i the polarizability of dipole i, $\mathbf{r}_i$ the radius vector of the ith dipole, and $\mathbf{G}$ the Green's tensor between dipoles i and j.

There are several expressions for β in Eq. (43) (e.g., Yurkin & Hoekstra 2007). In general, β is a function of k, m, and d. In the limit $kd \to 0$, the Clausius-Mossotti equation relates the polarizability of a cubic lattice of isotropic (spherical) dipoles to the relative permittivity of the lattice,

$$\beta_{\mathrm{CM}} = \frac{3d^3}{4\pi}\frac{\epsilon_r - 1}{\epsilon_r + 2}, \tag{44}$$

where it is assumed that the number density of dipoles $n_0 = 1/d^3$. Notice that when substituting the polarizability from the electrostatics theory for small spheres into Eq. (44), it yields the M-G formula for the effective permittivity (Eq. (42)).

Draine (1988) improved the polarizability description for finite kd by introducing the radiative-reaction correction in order to satisfy the optical theorem. He later refined the polarizability by requiring that the lattice reproduces the dispersion relation of a continuous medium with effective permittivity $\epsilon(\omega)$ (Draine & Goodman 1993). This is called the lattice dispersion relation (LDR), and it has become the most common description of the polarizability of dipoles in a lattice:

$$\begin{aligned}\beta_{\mathrm{LDR}} &= \frac{\beta_{\mathrm{CM}}}{1 + \frac{\beta_{\mathrm{CM}}}{d^3}[(b_1 + m^2 b_2 + m^2 b_3 S)k^2 d^2 - \frac{2}{3}\mathrm{i}k^3 d^3]}\\ b_1 &= -1.8915316, b_2 = 0.1648469, b_3 = -1.7700004\\ S &= \frac{1}{k^2 E_0^2}(k_x^2 E_{0,x}^2 + k_y^2 E_{0,y}^2 + k_z^2 E_{0,z}^2).\end{aligned} \tag{45}$$

It has been shown that the LDR formula loses accuracy for refractive indices $|m - 1| > 2$ (Yurkin et al. 2010). At microwave frequencies below 10 GHz, liquid water can have $|m - 1| > 7$. Filtered coupled dipoles (FCD) provides a better description of the polarizability

$$\beta_{\mathrm{FCD}} = \frac{\beta_{\mathrm{CM}}}{1 + \frac{\beta_{\mathrm{CM}}}{d^3}[-\frac{4}{3}k^2 d^2 - \frac{2}{3}\mathrm{i}k^3 d^3 - \frac{\ln((\pi - kd)/(\pi + kd))}{\pi}k^3 d^3]}. \tag{46}$$

Notice that $kd < \pi$ is required. In addition, the interaction term of point dipoles, i.e., the

Green's tensor, is replaced with the filtered Green's tensor

$$\begin{aligned}
\mathrm{G}^{FCD}(\mathbf{r}_i,\mathbf{r}_j) &= \mathrm{I}\left(k^2 g_F(R) + \frac{g_F'(R)}{R} + \frac{4\pi}{3}h_r(R)\right) + \frac{\hat{R}\hat{R}}{R^2}\left(g_F''(R) - \frac{g_F'(R)}{R}\right), \\
h_r(R) &= \frac{\sin(k_F R) - k_F R\cos(k_F R)}{2\pi^2 R^3}, \\
g_F(R) &= \frac{1}{\pi R}[\sin(kR)[\mathrm{i}\pi + \mathrm{Ci}((k_F-k)R) - \mathrm{Ci}((k_F+k)R)] + \\
&\quad \cos(kR)[\mathrm{Si}((k_F+k)R) + \mathrm{Si}((k_F-k)R)]], \qquad (47)
\end{aligned}$$

where $k_F = \pi/d$ is the wave number corresponding to the grid, $h_r(R)$ is the filter impulse response, $g_F(R)$ is the filtered scalar Green's function, and I is the identity tensor.

DDA is a flexible method for computing light scattering from arbitrarily shaped and inhomogeneous particles. Generally, there are two conditions that validate DDA. First, the dipole spacing relative to the internal wavelength must be small enough. Second, the number of dipoles must be large enough to represent the shape of the particle adequately. It is usually required that $|m|kd < 1.0$, but a more restrictive requirement $|m|kd < 0.5$ is given by Penttilä et al. (2007). At microwave frequencies, Teschl & Randeu (2009) recommend $|m|kd < 0.05$ for particles with liquid water. The choice of polarizability in Eq. (43) can have significant influence on the accuracy (Yurkin et al. 2010). The validity of DDA is discussed by, e.g., Draine (2008), Yurkin et al. (2006), Yurkin & Hoekstra (2007), and Zubko et al. (2010).

4.6 Exact vs. approximate methods

There are two types of accuracy with scattering models: accuracy of theory and accuracy of computation. The Mie theory is an exact theory for spherical particles, regardless of the size parameter or refractive index of the particle, whereas the Rayleigh approximation is an approximate theory for particles small compared to the wavelength. In practice, due to the limited accuracy of the floating-point arithmetic in computers and limited computational resources, the computational implementation of these scattering models have limitations not proposed by the theories. The practical limitations can also sometimes be more relaxed than specified by the theory, i.e., the Rayleigh approximation, which can produce adequate results up to $x \approx 1$. On the other hand, DDA is an approximate theory that can be applied to arbitrarily shaped particles, but its accuracy is determined mostly by the available computer resources.

Due to practical reasons, accuracy is usually not as important as efficiency. Efficiency is a computational property of an implementation. It is determined by the speed of computation and the amount of resources used, such as memory. The analytical solutions to scattering problems are almost always more efficient than the numerical ones. There are, however, only a limited number of cases, where there actually exists an analytical solution. Sometimes implementations of exact theories can provide results not possible with numerical methods, and this compromise between accuracy and efficiency is a necessary evil.

5 Polarization studies of wavelength-scale particles

5.1 Radiation problem

In a direct scattering problem, the incident field is known, the properties of the scatterer are known and the scattered field can be readily computed. However, this does not reveal the interaction between the incident field and the scatterer, or the interaction between different parts of the particle itself. It is therefore important to study how the internal field of the particle is distributed and how it relates to the scattered field. This can be achieved by solving an equivalent problem of radiation from a set of dipoles. DDA seems to be the most convenient method for this kind of study.

To obtain the internal field for a set of dipoles, the scattering problem must be solved first with DDA. The structure of the internal field depends both on the incident field ($\mathbf{k}$ and $\mathbf{E}_0$) and the properties of the scatterer. To study the relation between the internal field and polarization quantities of the scattered field, the scattering problem must be solved for two orthogonal incident polarizations defined with respect to the scattering plane (see Section 2.2). This produces two different internal field distributions for a given scatterer in a fixed orientation. They can be analyzed with respect to the scattered far-field components parallel and perpendicular to the scattering plane. This produces four independent quantities that are related to the elements of the amplitude scattering matrix (Eq. (9)).

The scattered field components in the far-field region can be derived from the internal field as,

$$\begin{aligned} E_{\|\mathrm{s}} &= \frac{\exp(\mathrm{i}kr)}{\mathrm{i}kr}[\mathbf{e}_{\|\mathrm{s}} \cdot \sum_{j=1}^{N} \mathbf{E}_j^{\mathrm{int}} \exp(-\mathrm{i}\mathbf{e}_{\mathrm{r}} \cdot k\mathbf{r}_j)], \\ E_{\perp\mathrm{s}} &= \frac{\exp(\mathrm{i}kr)}{\mathrm{i}kr}[\mathbf{e}_{\perp\mathrm{s}} \cdot \sum_{j=1}^{N} \mathbf{E}_j^{\mathrm{int}} \exp(-\mathrm{i}\mathbf{e}_{\mathrm{r}} \cdot k\mathbf{r}_j)], \qquad (48) \end{aligned}$$

where $E_{\|\mathrm{s}}$ is the scattered-field component parallel to the scattering plane, $E_{\perp\mathrm{s}}$ is the component perpendicular to the plane, $\mathbf{r}_j$ is the position vector of the jth radiating element, $\mathbf{E}_j^{\mathrm{int}}$ is the internal-field vector at position j, r is the distance from the particle to the observer in the far field, and N is the number of radiating elements inside the particle.

5.2 Methods of study

Given the internal field at discrete locations inside the scatterer, there are many ways to study the relation between the internal and scattered fields. One method is an active approach, in which the internal field is modified or switched off completely at certain locations inside the scatterer. For example, Zubko et al. (2006) studied the effect of modifying the dipole-dipole interactions in the DDA formulation on the degree of linear polarization. Muinonen et al. (2006) noticed that switching off the entire longitudinal component of the internal field of a spherical particle produced Rayleigh-like polarization. In Papers II, and III, the effect of switching off the entire longitudinal component of internal field is compared to the unmodified case. In Paper IV, only specific parts inside the scatterer are switched off. When the scattered field derived from the modified internal field is compared to the unmodified case, the difference between these cases gives information about the contribution of the selected locations inside the scatterer to the total scattering. However, it is not obvious, which locations to select for the study.

Since the total scattering is the result of interactions between all the radiating elements, it is difficult to decouple these interactions from the integrated scattering quantities. According to Eq. (48), the scattered field components depend both on the internal field amplitudes of the elements and the relative phases between them. In principle, each component in the summation can be considered as a partial wave originating from an element j and the total scattered wave as a superposition of them. The amplitudes describe the localized energy density of the partial waves, while the phases describe the interference between these waves. A similar interpretation is also used by Mishchenko et al. (2011).

If the elements that have the largest energy densities are switched off, it is evident that the differences between modified and unmodified cases are larger than when switching off the elements with lowest energy densities. This kind of study will therefore reveal the relative contribution of the elements to the scattered field characteristics. This can be achieved by first ordering the dipoles based on their local energy density, and computing the total energy density of all dipoles. Then, a cutoff value can be chosen, which is a fraction of the total energy density. A subset of the ordered dipoles, starting from the most brightest that have larger total energy density than the cutoff value, are called core dipoles. All other dipoles are called non-core dipoles (Paper IV). Then the cutoff value in percentage

$$\mathrm{cutoff} = 100 \cdot \frac{\sum_{\mathrm{i}=1}^{M} E^*_{\mathrm{int,i}} E_{\mathrm{int,i}}}{\sum_{\mathrm{i}=1}^{N} E^*_{\mathrm{int,i}} E_{\mathrm{int,i}}}, \tag{49}$$

where M is the number of core dipoles.

Notice that switching off the internal field for certain element is not the same as removing the element entirely from the scatterer. The latter approach modifies the shape, which has a strong influence on the distribution of internal field due to the interaction between the elements. It has an unpredictable effect on the scattered field, and would invalidate the comparison. In the former approach, only the local internal field is modified keeping shape intact. This ensures that all else is fixed, when the scattered field of modified and unmodified cases are compared. This kind of method is analogous to a phased array, which is a group of antennas that can be controlled separately to get a desired far-field pattern for the whole antenna (e.g., Visser 2005). In this case, the individual antennas correspond to the elements that can be switched off.

Two partial waves that have the same amplitude but opposite phase will always interfere destructively and produce no contribution to the superposition (Eq. (48)). Waves with the same phase interfere constructively and produce enhancement/no cancellation. Extending this principle to all elements in a given line or a plane therefore gives information about the interference phenomena that are occuring between the partial waves from the elements. Given a set of internal-field amplitudes and phases, this provides a method to compute integrated maps of the internal-field energy densities. In the method, the three-dimensional field is projected to a two-dimensional image plane by adding the complex internal-field amplitudes along the scattering direction including the relative phase of the radiating elements/dipoles in the far field. For each point/pixel in the image plane, this produces a complex vector representing the far-field amplitudes of the entire line of dipoles in Eq. (48). In this way, the contribution from each line of dipoles to the far-field scattering characteristics can be analyzed independently from each other. In addition to the integration of the line of dipoles, one additional integration of the dipole planes can be made in two orthogonal directions, $\hat{\mathbf{e}}_\theta$ and $\hat{\mathbf{e}}_\phi$, producing two profile curves for the particle. By further integrating these planes into one complex vector for the whole particle, the total scattered field amplitude is obtained. In addition to the energy density, the phase can also be included in the profile curves to reveal destructive and constructive interferences between the lines/planes of dipoles.

For polarization studies, the internal field must be computed for two orthogonal incident polarizations for each sample particle (Sect. 2.2). Notice that in order to resolve phase information from the internal field, the particle must be in a fixed orientation. Any averaging of the localized fields will make the phase information ambiguous and results in a loss of information. This is analogous to the relation between the **S** (Sect. 2.4) and **F** (Sect. 2.3) matrices, where the imaginary representation of the scattering system is transformed into a real form using the Stokes/Mueller formalism. There is no loss of information in the case of a single particle in a fixed orientation. However, when computing scattering from a medium of different particles in different orientations, as in the case of a planetary regolith or the Earth's atmosphere, the number of independent terms in the scattering matrix decreases, and leads to a loss of information of the individual particles. This means that phase information cannot be used when studying the internal fields of a mixture of particles.

5.3 Mechanisms for polarization phenomena

The internal field of a scatterer is determined by both the properties of the scatterer and the incident field. For a given particle, the propagation direction and the polarization of the incident field determine the localized distribution of the internal field. It is therefore convenient to divide the internal field into components that are defined with respect to the incident wave reference frame. The longitudinal component of the internal field is defined as the component parallel to the incident propagation direction specified by the wave vector of the incident field, while the transverse components of the internal field are defined as the two orthogonal components parallel to the two orthogonal polarizations of the incident field. This definition was introduced in Paper I.

Wavelength-scale scatterers interact strongly with the incident electromagnetic wave, because the size of the scatterer is no longer smaller than the wavelength and the incident electromagnetic field can no longer be considered to be homogeneous inside the scatterer. The internal field structure of wavelength-scale scatterers can partly be understood by an analogy to the geometric optics approximation (GOA), i.e., particles large compared to the wavelength. Due to the surface curvature and the dielectric nature of the scatterer, a phase shift is produced between the internal and incident waves. Because this phase shift is larger for the waves going through the center than those going through the perimeter, it produces a circular internal wave front with the focal point at the forward part of the particle. The apparent wavelength λ/m of the internal wave is determined by the refractive index of the particle. As these waves are focused to the forward part of the scatterer, they produce concentrated regions of the internal-field energy density. These regions are sometimes called 'hot spots' and they are very prominent for regular particles (Owen et al. 1981, Benincasa et al. 1987, Barton 2002, Astafyeva & Babenko 2004, Li et al. 2005). This focusing of light is also the defining feature in optical lenses. Fuller (1991) demonstrates that, for larger size parameters ($x = 50$), the maximum local energy density is shifted to the forward part of the near field, and that such particles can be used as lenses. The studies presented in Papers II and IV demonstrate that this focusing effect can be extended to the interiors of wavelength-scale particles. It is interesting to hypothesize that, in principle, this focusing could heat up the particles from the inside and modify their internal structure, maybe even fracture them.

It should be noted that the interpretation for the internal-field structure can be misleading. Although the refractive index is used to represent the electromagnetic properties of the particle regardless of its size parameter, i.e., from the Rayleigh approximation to wavelength-scale to GOA, it manifests itself differently in these regimes. For single dipoles, it determines the induced dipole moment and is a direct response of the matter to the applied field (see Sect. 4.1). For large particles, it determines the direction of the refracted wave. This change in direction is due to the change in the speed of the electromagnetic wave. The interaction of the wave with the particle is localized and because of this, mostly the boundaries and surfaces of particles define the scattering quantities. For wavelength-scale particles, both of these explanations are inaccurate. The local field inside the particle is the result of all interactions between the radiating elements of the particle following the incident-field response. Due to this non-localized property of the internal field for wavelength-scale particles, the analogy is inaccurate.

In addition to the propagating distorted wave focused to the forward part of the particle, there is a circular pattern of local maxima located near the perimeter of the particle seen for both the longitudinal and transverse components. Due to the regular phase structure of the maxima, the circular pattern can be interpreted as a standing wave with waves propagating in opposite directions along the perimeter, always forming roughly x number of maxima and minima. This also follows from geometry: the maximum circumference of a spherical particle is $p = 2\pi a = x\lambda$. For each wavelength, there is one maximum and minimum amplitude making $2x$ energy density maxima in total. The apparent wavelength of this standing wave corresponds closely to the external wavelength due to the proximity to the surface and the boundary conditions for electromagnetic waves.

An example of the three-dimensional structure of the internal field for a spherical particle with size parameter $x = 8$ and the refractive index $m = 1.55$ is given in Fig. 10.

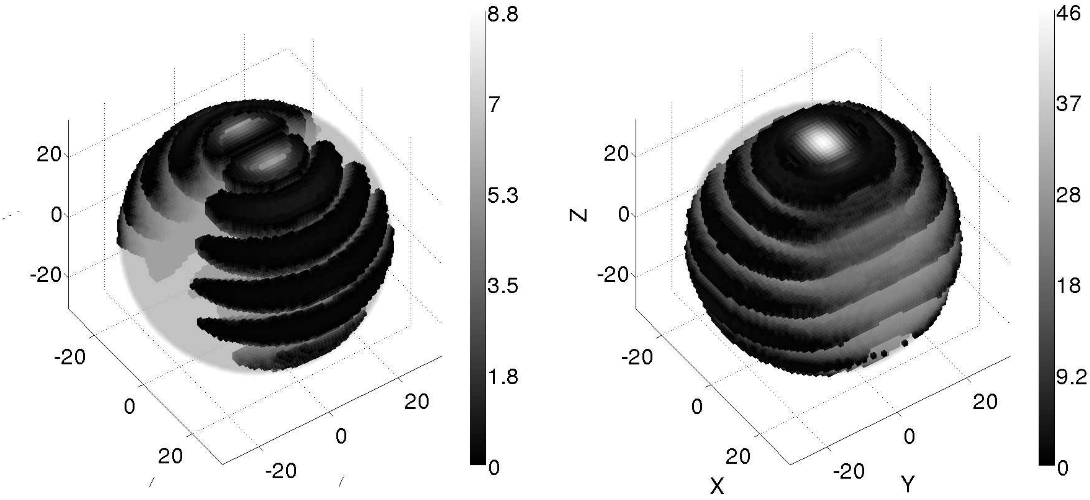

Figure 10: The local energy density distributions for the longitudinal (left panel) and transverse (right panel) component of the internal field for a spherical particle using 90% cutoff (core dipoles). The size parameter is $x = 8$ and the refractive index $m = 1.55$. The incident wave is X-polarized and propagating in the positive Z-direction. Non-core dipoles have been made slightly transparent.

In the next sections, the longitudinal and transverse components are discussed in more detail to better understand the internal field structure of wavelength-scale particles. A spherical particle is used as an example.

5.3.1 Longitudinal component of the internal electric field

Since the longitudinal component is parallel to the wave vector of the incident field, it is always in the scattering plane, which is defined by the wave vectors of the incident and scattered field. This means that it does not contribute to the perpendicular component of the scattered field. For the parallel component, its contribution varies as a function of the scattering angle. In the far field, the scattered wave is transverse, i.e., perpendicular to the direction of propagation defined by the wave vector of the scattered field. Because of this, there is a geometric factor $|\hat{\mathbf{e}}_{\|\mathrm{s}} \cdot \hat{\mathbf{e}}_{\mathrm{z}}| = \sin\theta$ (assuming that the wave is propagating along the positive Z-axis) in the scattered field originating from the longitudinal component. At the 90° scattering angle, the factor equals one, and decreases to zero towards the forward and backward scattering directions, giving the largest contribution to the scattered field at intermediate scattering angles.

For a symmetric particle, such as a sphere, the distribution of the longitudinal component is also symmetric (e.g., Ren 1994). This is seen in Fig. 11, which shows the distribution of the normalized energy density of the longitudinal component only. The phase, which is coded in color according to Fig. 11 (bottom panel), is also shown. For a given incident polarization, there is an odd parity (opposite phase) with respect to the central plane that is perpendicular to the incident polarization. Because of the symmetry, there is no net-longitudinal component for spherical particles, and other particles rotationally symmetric with respect to the wave vector of the incident field. Therefore, any non-Rayleigh-like polarization characteristic must be due to interference between the partial waves of the scatterer.

Whether the incident field is polarized either parallel or perpendicular to the scattering plane, two concentrated areas or internal field extrema are formed at the forward part of the particle (Fig. 11; left) that are located in the plane defined by the incident polarization and propagation direction. These maxima are separated by about half a wavelength, and have opposite phases. When the incident field is polarized parallel to the scattering plane, at intermediate scattering angles (near the X-axis direction), the partial waves originating from these extrema interfere constructively and produce enhancement for the parallel component of the scattered field. The two extrema do not contribute to the perpendicular component in this reference frame. When the incident field is polarized perpendicular to the scattering plane, these extrema are the same as for the parallel case, but are located perpendicular to the scattering plane. In this case, the extrema interfere destructively at all scattering angles, and do not contribute to the scattered field. For an unpolarized incident wave, the scattered field is averaged over two polarizations of the incident field, and due to the constructive interference for the parallel component, the degree of linear polarization $P = (E_\perp E_\perp^* - E_\| E_\|^*)/(E_\perp E_\perp^* + E_\| E_\|^*)$ is mostly negative at intermediate scattering angles. This was shown in Papers II and III, where the degree of linear polarization became almost Rayleigh-like as the entire longitudinal component is switched off. Near the backscattering direction, switching off did not have much of an effect, because of the geometric factor for the longitudinal component. In Paper IV, it was shown that, at intermediate scattering angles, switching off the longitudinal component only for the core dipoles (elements with the largest energy densities) increased the degree of linear polarization substantially, when compared to the unmodified cases. It was concluded that only about 5% of the dipoles are responsible for the negative polarization at intermediate scattering angles.

For irregular particles, the distribution of the internal field is no longer symmetric due to the irregular surface. Because of this, there is a net-longitudinal component at intermediate scattering angles. This will enhance the parallel component of the scattered field and produce negative polarization at intermediate scattering angles. However, ac-

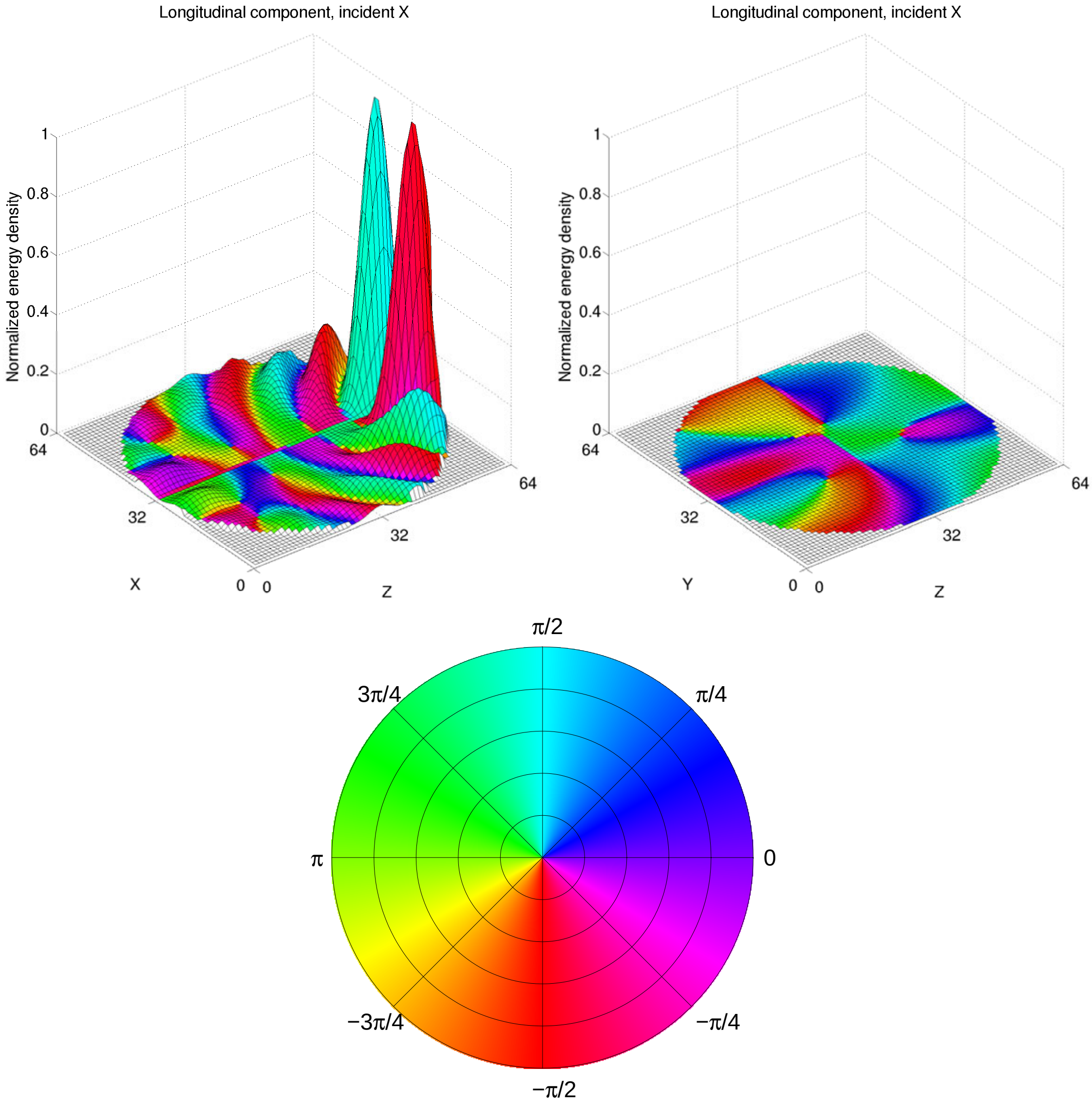

Figure 11: The normalized energy density at the central $X-Z$ (top left panel) and $Y-Z$ (top right panel) planes for the longitudinal component, when the incident wave is X-polarized, i.e., parallel to the scattering plane ($X-Z$). The incident wave is propagating along the positive Z-axis. The size parameter is $x = 8$ and the refractive index is $m = 1.55$. The color coding for the phase is shown in the panel at the bottom.

cording to the results in Paper IV, the contribution from the interference between the partial waves to the enhancement is also significant for irregular particles. This means that the irregular surface does not completely destroy the regular structure of the internal field. The results in Paper IV did show that, as irregularity increases, the amount of negative polarization decreases. In Paper III, when the entire longitudinal component was switched off, polarization became generally more positive for a GRS particle than for a sphere with the same size parameter and refractive index. This can be explained by a weaker interference between the partial waves for nonspherical particles.

5.3.2 Transverse component of the internal electric field

By definition, the transverse component is always in the plane perpendicular to the propagation direction of the incident wave. It is therefore also the main component in the internal fields. Because the scattering problem is solved for two orthogonal polarizations of the incident field, the transverse component always contributes to both the parallel and perpendicular components of the scattered field. In the far field, the largest contribution comes from scattering angles near the forward and backward directions with the smallest contribution at the 90° scattering angle (contrary to the longitudinal component). This is due to the geometric factor $|\hat{\mathbf{e}}_{\|\mathrm{s}} \cdot \hat{\mathbf{e}}_{\|\mathrm{i}}| = \cos\theta$ for the case with the polarization of the incident field parallel to the scattering plane. When the polarization of the incident field is perpendicular to the scattering plane, it has the same contribution to the scattered field at all scattering angles.

Just as for the longitudinal component, the distribution of the transverse component is symmetric for particles that are rotationally symmetric with respect to the polarization of the incident field (Fig. 12). Instead of two prominent maxima, as for the longitudinal component, there are several local maxima formed as a wavelike pattern with one prominent maximum at the forward part of the particle. According to our interpretation in Paper V, the maxima around the perimeter form a standing wave pattern with every other maximum being in phase. This standing wave is formed by two waves propagating in opposite directions along the perimeter. In addition to the standing wave, there is a central forward propagating wave. Due to the boundary conditions for an electromagnetic wave (Sect. 2.1), the separation of the maxima are about half of a wavelength around the perimeter of the particle. Near the center, the wavelength decreases by a factor of $1/m$ according to the refractive index, which corresponds to a total phase shift $2x|m-1|$ with respect to the incident wave (van de Hulst 1957).

Notice that in the plane parallel to the polarization of the incident field (Fig. 12; left), only the central wave is present, whereas in the plane perpendicular to the incident polarization (Fig. 12; right), the standing wave pattern is clearly visible in addition to the central wave. In Paper V, the far-field mapping of this regularly placed ring of maxima is described as 'an interference dial'. The number of both maxima and minima for the half circle equals roughly, but not exactly, to the size parameter of the particle (e.g., in the case of Fig. 12, it is 9). This pattern can also be seen in Paper II for other size parameters. In Paper V, this pattern is shown to be responsible for the non-Rayleigh-like interference features, such as NPBs, observed for wavelength-scale particles at certain scattering angles. For spherical particles, the pattern is very symmetric, which results in large negative and positive values for the degree of linear polarization due to an almost complete destructive/constructive interference between the partial waves originating from the maxima.

In the exact backscattering direction, it is clear that due to the pairwise symmetry of the maxima the partial waves interfere constructively. Rotating the dial by a sequence of quarters of a wavelength $\lambda/4$, here λ corresponding to the apparent wavelength between the maxima, along the perimeter is the same as rotating the scattering wave vector by a certain angle. This equals to a change in the scattering angle by $\Delta\theta = 2\pi/(4 \times 9) = \pi/18$. This follows closely to the angular interval of maxima and minima in the total intensity seen in Fig. 9 (left). In this geometry, the partial waves interfere destructively with almost pairwise cancellation for $I_\perp$ (Fig. 12; right), which is seen in P as a deep negative peak near the backscattering direction (Fig. 9; right). When rotating another quarter of a wavelength, there is pairwise enhancement, which is seen as a positive peak in P. Continuing this rotation, all peaks in P can be traced to a rotation in the interference dial. It should be noted that since the degree of polarization is the ratio of two angularly varying quantities, $\Delta\theta$ does not exactly match the interval seen for P. Nevertheless, based on the results in Papers II, III, IV and V, there is a clear dependence between the distribution of the internal field energy density and the angular far-field scattering features. The success of the interference rules, presented in Paper V, to determine the particle size parameters, refractive indices, and shape from the scattered field characteristics, further reinforces the idea that there is a clear connection, at least for simple shapes.

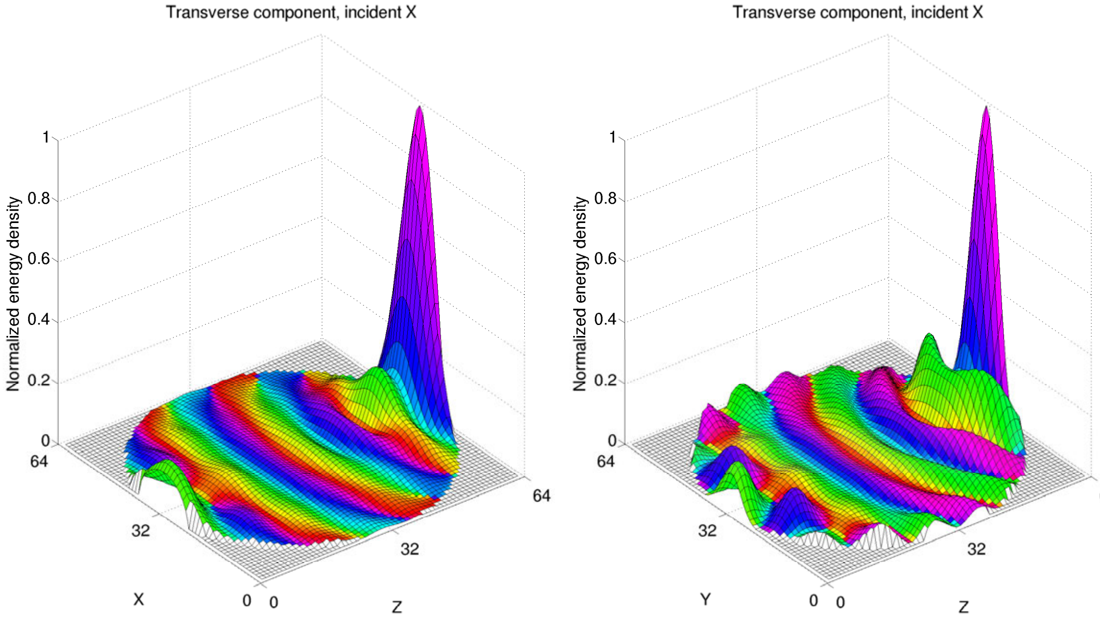

Figure 12: Same as in Fig. 11, but for the transverse component. Color coding for the phase is also shown in Fig. 11.

For irregular particles, this connection becomes more complicated since there is no simple way to describe an irregular particle. In Paper IV, it was evident that the distribution of energy density for the internal field depends greatly on the exact shape of the particle. It was also shown that there is a clear connection between the maxima of the longitudinal component and the negative polarization at intermediate scattering angles. Therefore, generalizing the interference rules to irregular particles seems to require an extensive amount of work. In principle, the tools that were developed for the studies in the thesis can be used for particles of any shape and composition. In practice, the analysis of a single shape can be time consuming making a more comprehensive study currently infeasible.

5.4 Case study: snowflakes at microwave frequencies

The results of Paper VII indicate that, for wavelength-scale particles, the shape of the particle is an important parameter, especially for fluffy structures. Trying to replace a realistic snowflake shape with an equivalent spheroidal particle seems to fail at least for the backscattering quantities. A similar conclusion for fluffy particles is also given by Nousiainen, Kahnert & Lindqvist (2011). This discrepancy between the shape models can be analyzed with the tools developed previously for Papers IV and V. Here, a new study is presented, where these tools are applied to a snowflake at the W band (94 GHz).

In this study, one example aggregate snowflake shape is used to compute the internal field at each dipole site with DDA. The sample is chosen according to the maximum size parameter $x = 3.2$, which happens to coincide with the first interference minimum for the backscattering cross section (Fig. 6 in Paper VII). A spheroid with the same size, aspect ratio, and orientation is also used to compute the internal fields with DDA. For the spheroid, the mixture of ice and air is handled by computing the effective refractive index using the M-G EMA. The particle can therefore be characterized as soft due to the presence of air inside it.

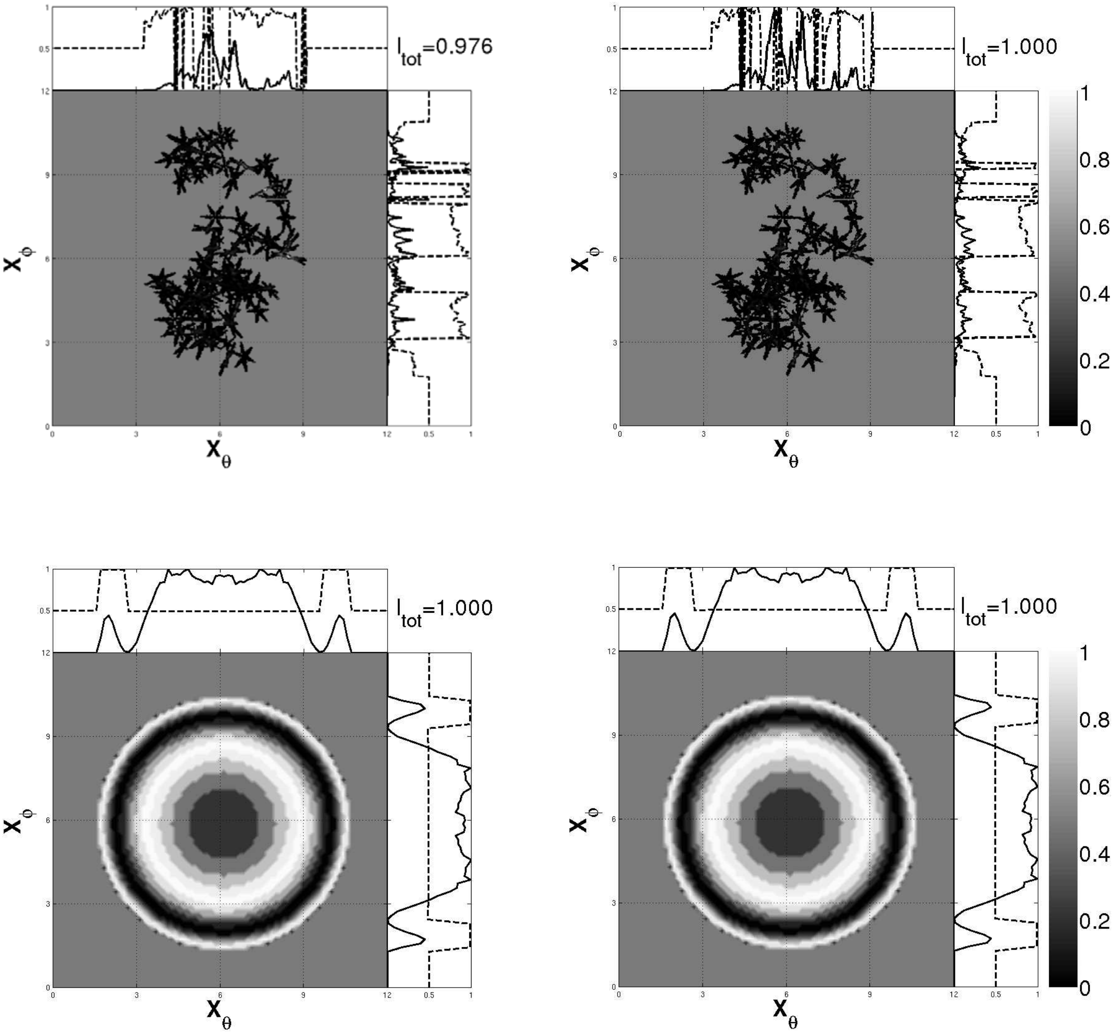

Figure 13: The copolarized contributions from the internal fields to the backscattering far-field at the W band for an aggregate of 100 ice crystals (top panels) and a similar sized soft-spheroid particle (bottom panels). On the left panels, the incident field is polarized parallel to the scattering plane (vv), and on the right panels, perpendicular to the scattering plane (hh). The maximum size parameter $x = 3.2$. The refractive index of the aggregate is $m = 1.7844 + \mathrm{i}0.0021$. The effective refractive index of the spheroid is $m_{\mathrm{eff}} = 1.0005 + \mathrm{i}0.000001$.

Fig. 13 shows the far-field backscattering contributions from the internal fields of a realistic snowflake (top panels) and a soft spheroid (bottom panels) using the integrated map tool developed previously (Sect. 5.2). From the top panels it is clear that the fluffy structure of snowflakes causes the internal field to be generally weak and unfocused. There are no local bright maxima typical for solid shapes. The largest far-field contributions are located at the parts with a concentration of ice crystals. In addition, the phases between the different parts of the snowflake seem to be almost random, which is seen as a large oscillation in the curves on the top and on the right (dashed line). Due to the irregular shape, there is a small difference in the total backscattered intensity between the parallel (top left panel) and perpendicular (top right panel) component shown as a number in the top right corner in each panel.

For the soft spheroid (bottom panels), the structure of the internal field is completely different as compared to the aggregate snowflake (top panels). There are two bright rings, a narrower ring near the perimeter and a wide ring near the center. The phase of these rings is opposite, which again can be seen in dashed lines in the curves on the top and on the right. Because of this, there is destructive interference/partial cancellation between the partial waves originating from the outer and inner rings in the exact backscattering direction. This decreases the backscattering cross section of the soft spheroids relative to the aggregate (Fig. 6 in Paper VII). To verify this, another soft spheroid is chosen with maximum size parameter $x = 4.5$, which does not show the interference feature. The integrated maps for the particle are shown in Fig. 14. As can be seen, there is one wide ring near the perimeter and a small maximum at the center. Again, the ring and the maximum are in opposite phase, but due to the relatively small contribution of the central maxima compared to the ring, the destructive interference/cancellation is diminished. To conclude, the reason between the difference in backscattering cross sections of soft spheroids and aggregates is destructive interference inside the spheroid. In fact, this study proposes that the oscillating maxima and minima present for the backscattering cross sections as size parameter increases, for spherical/spheroidal particles, is due to this same interference mechanism. The interference rules presented in Paper V can be applied to specify the locations for these features.

Since the phase structure of the internal fields in wavelength-scale snowflakes is to a large extent random, it is evident that the interaction between the elements is small as compared to the response to the incident field. This leads to the Rayleigh-Gans approximation (RGA), where the near-field interaction between the elements is neglected and only the far-field interference is taken into account. The agreement between RGA and DDA for fluffy snowflakes has already been verified by Westbrook et al. (2006). They also demonstrated the inability of the soft-sphere model to estimate backscattering cross sections at high microwave frequencies.

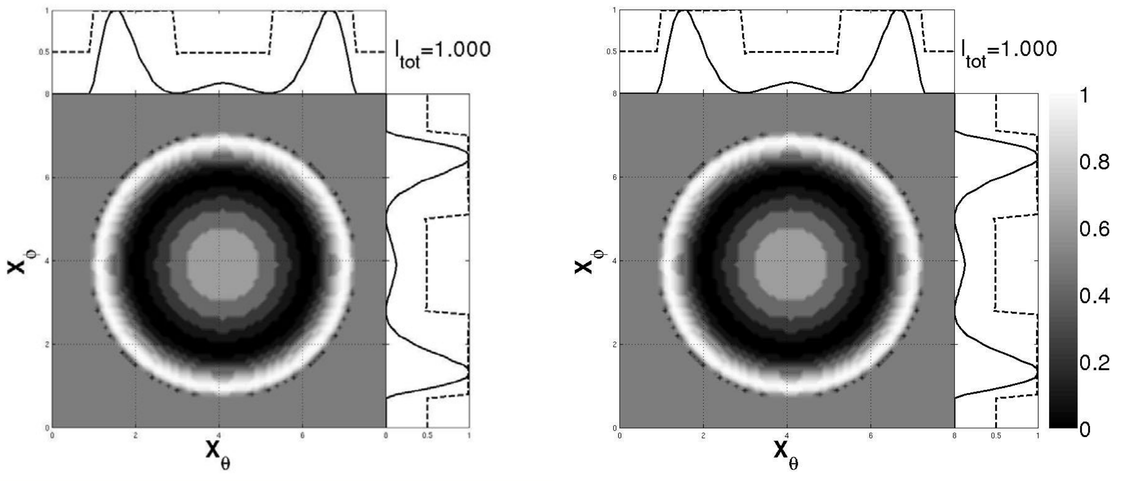

Figure 14: Same as in Fig. 13, but for a soft-spheroid particle with maximum size parameter $x = 4.5$.

6 Summary of papers

6.1 Paper I

Light scattering by Gaussian random particles with discrete-dipole approximation. The scattering by wavelength-scale GRS particles is studied for various size parameters and refractive indices. It is found that there are four ubiquitous phenomena for the scattering characteristics: an enhancement for the phase function towards the exact backscattering direction, a systematic NPB near backscattering, a double-lobe feature for the depolarization ratio (Lindqvist et al. 2009), and interference maxima at intermediate scattering angles. Also, the polarization norm, polarization asymmetry parameter, the phase-function asymmetry parameter, and the degree of linear polarization for GRS particles are compared to spherical particles with the same size parameters and refractive indices. It is found that there are significant differences depending on the physical parameters, especially for larger sizes and refractive indices. Increasing σ (Sect. 3.2) also increases the differences. A new mechanism based on the internal fields to interpret the scattering characteristics is also presented.

6.2 Paper II

Interrelating angular scattering characteristics to internal electric fields for wavelength-scale spherical particles. In this paper, we use the Lorenz-Mie theory and discretize the internal electric field of spherical particles into small elements. The longitudinal component is studied by switching it off entirely for the elements, and comparing the scattered field characteristics between the exact (unmodified) and modified cases. The transverse components are studied by dividing the particle interior into cells, and computing the corresponding radiation scattering characteristics for the particle incoherently. This eliminates the interference of the partial waves between the cells, and shows the contribution of the transverse components to scattering when compared to the exact solution. It is found that, for particles with $|m| > 1$, both the longitudinal and transverse components are concentrated in the forward part of the particle, while for $|m| < 1$ they are concentrated in the backward part. For the more absorbing case ($m = 2 + 2\mathrm{i}$), the internal field is concentrated near the surface. When the entire longitudinal component is switched off, the degree of linear polarization becomes more positive overall. When the interior is also divided into four incoherent parts, the polarization becomes positive for all scattering angles, except for large ($x > 4$) particles, which still shows the negative polarization branch near backscattering. When the interior is further divided into sixteen incoherent cells, polarization becomes positive for all studied cases, and the resulting polarization curve is almost Rayleigh-like. It is concluded that the longitudinal component has a strong contribution to the negative polarization over a wide range of scattering angles, while the transverse component dominates near the backscattering angle. The transverse component is also seen to be responsible for the backscattering peak.

6.3 Paper III

Interrelating angular scattering characteristics to internal electric fields for Gaussian-random-sphere particles. This paper is continuing the study of Paper II by applying the same methods to wavelength-scale GRS particles. It is found that for both $m = 1.55$ and $m = 1.33$ cases, the same mechanisms that were investigated in Paper II for spheres, can also explain the polarization characteristics of Gaussian-random-sphere particles. The negative polarization at intermediate scattering angles is explained by constructive interference between two opposite maxima of the longitudinal component that are separated by about half a wavelength at the forward part of the particles. It is also suggested that interference is weaker for the Gaussian-random-sphere particles than spherical particles, because the division into four incoherent cells is enough to eliminate any negative polarization, which is not the case with spherical particles.

6.4 Paper IV

Interpretation of single-particle negative polarization at intermediate scattering angles. Papers I, II, and III concentrate on studying the origin of the negative polarization for single wavelength-scale particles. This paper concentrates on the longitudinal component of the internal field, and provides a more thorough understanding of the polarization characteristics associated with it. The degree of linear polarization is studied for spherical, Gaussian-random-sphere and agglomerated debris particles by switching off the longitudinal component from core, noncore, and random dipoles. These are defined by a preset cutoff value from the total energy density of all dipoles after the dipoles are arranged according to their energy densities. This allows to locate the dipoles that have the largest contribution to the longitudinal component. It is found that a relatively small number of core dipoles contribute to the negative polarization at intermediate scattering angles. For both Gaussian and debris particles, it is about 5% of all dipoles. The interference between the partial waves is studied using two approaches. In the first approach, the core dipoles are switched off separately for the two incident polarizations. It is found that interference has a large contribution in scattering characteristics for irregular particles similar to spheres. In the second approach, interference is studied using integrated maps of the energy densities. It is shown that there is mostly constructive interference for the parallel component between the partial waves originating from the bright areas for all the different shapes studied. It is concluded that negative polarization near backscattering and the double-maximum feature in the depolarization ratio are due to the transverse component of the internal field.

6.5 Paper V

Polarization of light backscattered by small particles. In this paper, the linear polarization characteristics at the backscattering regime for spherical, cubic, spheroidal, and clusters of four spherical particles are studied using size parameters $4 \leq x \leq 10$ and refractive indices $1.1 \leq m \leq 1.9$. In addition, spherical and spheroidal particles in random orientation are studied using the same method as in Paper IV. It is found that the internal field of wavelength-scale particles is a combination of a standing wave near the perimeter and a distorted plane wave with the wavelength controlled by the refractive index of the particle along the central axis and changing to the incident wavelength near the perimeter of the particle. The circular wave-like pattern near the perimeter of the particle is interpreted to be a standing wave, which is formed in the plane perpendicular to the incident polarization. Its contribution to the scattered field can be characterized as an 'interference dial', which selects at certain scattering angles either pairwise destructive or constructive interference between the maxima in the wave pattern. In addition, new interference rules for the negative and positive polarization extrema in the degree of linear polarization are presented, which can provide a way to invert physical properties of the particles from their scattering characteristics.

6.6 Paper VI

Modeling C-band single scattering properties of hydrometeors using discrete-dipole approximation and T-matrix method. In this paper, polarization radar quantities are investigated at the C-band for spherical and spheroidal ice particles, as well as clusters of spherical ice particles that contain liquid water. The main purpose of this paper is to investigate the applicability of DDA to model scattering from these particles when compared to exact theories. It is found that for homogeneous particles, e.g., pure ice or pure water, DDA agrees well with the exact theories. For water-coated ice particles, there can be relative errors about 25% in the backscattering cross sections and larger for the extinction cross sections. The errors in the extinction are mainly due to the errors in the absorption. The reason for the errors is too small a grid for the coating. The agreement between DDA and the superposition TMM for a random cluster of ten ice spheres is good, but for clusters with 30% water, there can be almost 9% relative error in the backscattering cross sections, and 27% error in LDR_{vh}. It is suggested that, for clusters of spheres containing water, increasing the grid size for the constituent spheres should greatly improve the accuracy. It is also found that using filtered coupled dipoles as the polarizability in DDA effectively doubles the accuracy for spherical particles containing only water.

6.7 Paper VII

Radar backscattering from snowflakes: comparison of fractal, aggregate, and soft-spheroid models. Three different snowflake models; namely, fractal, aggregate, and soft-spheroid models, are used in this paper to compare their polarimetric radar quantities and applicability in the C-, Ku-, Ka- and W-bands. It is found that the polarimetric radar quantities agree well between the fractal and aggregate models for all the studied frequencies. The soft spheroid model agrees fairly well at the C- and Ku-bands, but underestimates the cross sections by a factor of 10 at the Ka-band, and a factor of 50-100 at the W-band. For the linear depolarization ratio, there are consistent differences between fractals and aggregates, as well as aggregates and spheroids.

6.8 Author's contribution

This section describes the author's contribution in the papers of the thesis. In Paper I, I carried out all the Mie scattering computations and the comparative study between the GRS and spherical particles. In Papers II-IV, I analyzed the results and made all the plots. In Paper II, I wrote a Mie scattering code using Fortran 90, which computes the internal electric and magnetic fields at discrete locations inside the scatterer, and outputs them in a file for analysis. I also implemented the code for the internal field modification together with K. Muinonen. I used these codes to compute the Mie scattering results in Papers I and II. In Paper III, I used the same codes as in Paper II, and applied them to the DDA computations by E. Zubko. In Paper IV, I wrote a visualization program for the integrated energy density maps using Matlab. The computations were performed with the DDA code by E. Zubko. In Paper V, I carried out computations for the spherical and spheroidal particles using TMM, and made all the scattering plots. I also computed the integrated energy density maps, using the ADDA code by Yurkin & Hoekstra (2011), and the visualization program, provided text to the introduction and helped to analyze the results. In Paper VI, I carried out all computations using the ADDA code, the TMM code by Mishchenko (1991), and the superposition TMM code by Mackowski & Mishchenko (1996), and analyzed the results. In Paper VII, I implemented all the shape models, and made the program to compute the physical properties of the generated particles. I also improved the fractal and aggregate models to include preferential orientations. I carried out all the DDA computations using ADDA, and J. Leinonen provided the TMM computations. I analyzed the results.

7 Conclusions and future prospects

The thesis shows that the non-Rayleigh-like features in the scattering quantities seen for wavelength-scale particles with varying shapes and refractive indices are due to the interference between the partial waves originating from certain parts of the particle interior. These parts can be identified by concentrations of local energy densities. The contributions from these parts to the scattered field can be analyzed using different methods, such as switching off the most contributing parts and comparing the scattered field to the unmodified case, or by using partial integration maps to identify destructive/constructive interference between the partial waves.

Because the structure of the internal field is determined by the incident polarization and propagation directions, as well as the physical properties of the particle, it was proposed in Paper I that it is convenient to divide the internal field into two components: the longitudinal and transverse components. From the results in Paper II and III, it is clear that the longitudinal component contributes mostly at the intermediate scattering angles, while the transverse component at the forward and backward scattering angles. In Paper IV, the longitudinal component was studied in more detail, and the studies showed that even for irregular particles, such as GRS and AD particles, the internal field is largely focused on the forward part and interference from the partial waves is not diminished totally by the irregular surface. It was also shown that only about 5% of the dipoles contribute to the negative polarization at intermediate scattering angles.

The physical interpretation of the interference mechanism is as follows: as the incident wave front reaches the particle, it is refracted in a sense that the wave fronts at different locations on the particle surface undergo different relative phase shifting due to the relative refractive index of the particle. This refracted wave front is focused on the forward part of the particle. It is also evident from the internal field structure of spherical particles, shown in Papers II and V, that some partial waves are not transmitted through the particle, but go around the particle in opposite directions, and form a circular standing wave near the perimeter. The size parameter of the particle seems to determine the number of maxima forming for the standing wave pattern. For the transverse component, this pattern is stronger in the plane perpendicular to the incident polarization (Paper V), while for the longitudinal component, it is always in the plane parallel to the incident polarization (Paper IV). At least for the spherical particles, this means that the NPB near the backscattering direction in the degree of linear polarization is due to the destructive interference for the perpendicular (transverse) component, while the negative polarization at intermediate scattering angles is due to the constructive interference for the parallel component (longitudinal). In addition to the NPBs, the mechanism presented in the thesis also explains the enhancement of the phase function near the backscattering direction and the double-lobe feature for the depolarization ratio (Paper V).

One interesting aspect of the studies is that the characteristics in the degree of linear polarization for simple shapes, such as spheres, spheroids, cubes, and small clusters of spheres, are similar for different size parameters and refractive indices. These non-Rayleigh-like characteristics begin near the size parameter $x = 2$ and become more numerous as the size increases. This behavior can be understood by the interference mechanism for the internal fields. It has been shown that the number of maxima for the standing wave equals roughly the size parameter. For $x = 2$, there are only two maxima; a minimum and a maximum for the amplitude of the standing wave. This is the shortest possible standing wave that can form inside the particle. As the size is increased, more maxima are generated, and this seems to continue even for particles large as compared to the wavelength. The interference patterns in the scattered field for wavelength-scale particles can be understood by the interference dial, and the locations for the maxima and minima can be determined from the interference rules presented in Paper V, at least for simple nonspherical particles. It is under study, how these can be applied to irregular particles. Nevertheless, the interference mechanism seems to be valid for particles with rough surface as was shown in Papers III and IV.

One area of research that seems to benefit from these mechanisms is the modeling of hydrometeors at microwave frequencies. For high frequencies, typical for space-borne radars, the sizes of hydrometeors, especially snow particles, are wavelength-scale. Due to their dielectric nature, all the results from the internal field studies are also applicable to these particles. However, since snowflakes are very fluffy in structure, this means that the internal field is not focused and can be almost random in phase resulting in weak interference features in the scattered field. For solid, homogeneous particles it is clear that the incident field is focused and the interference between the partial waves produces distinct features in the scattered field. This is evident from the results in Papers VI and VII. It is this difference in the shape and structure between the models that should be taken into account when modeling backscattering by snowflakes at microwave frequencies. The first results, when applying the Rayleigh-Gans approximation to snowflakes, have already shown that the interactions between the dipoles can be neglected to a large extent. We plan to investigate this in more detail and produce a simpler scattering model that can be applied to fluffy structures at wavelength-scale sizes.

One question for explaining the negative polarization still remains: what is the relationship between CBM and the mechanisms presented in Papers I–V? It would be important to find the answer to help interpret the remote sensing observations from atmosphereless solar-system bodies. Hopefully this can be answered in our future studies. One thing is certain; we must first look at the direct problem in detail before being able to make realistic assumptions for the inverse problem. With the help of the tools and interpretations that were developed for the studies in the thesis, this should be feasible.

References

Aden, A. L. & Kerker, M. (1951), ‘Scattering of electromagnetic waves from two concentric spheres’, *J. Appl. Phys.* **22**, 1242–1246.

Asano, S. (1983), ‘Light scattering by horizontally oriented spheroidal particles’, *Appl. Opt.* **22**, 1390–1396.

Astafyeva, L. G. & Babenko, V. A. (2004), ‘Interaction of electromagnetic radiation with silicate spheroidal aerosol particles’, *JQSRT* **88**, 9–15.

Atlas, D., Kerker, M. & Hitschfield, W. (1953), ‘Scattering and attenuation of non-spherical atmospheric particles’, *J. Atmos. Terr. Phys.* **3**, 108–119.

Austin, P. M. & Bemis, A. C. (1950), ‘A quantitative study of the ”bright band” in radar precipitation echoes’, *J. Meteor.* **7**, 145–151.

Aydin, K., Seliga, T. A. & Balaji, V. (1986), ‘Remote sensing of hail with a dual linear polarization radar’, *J. Appl. Meteor.* **25**, 1475–1484.

Barton, J. P. (2002), ‘Electromagnetic field calculations for an irregularly shaped, near-spheroidal particle with arbitrary illumination’, *J. Opt. Soc. Am.* **19**, 2429–2435.

Battaglia, A., Ajewole, M. O. & Simmer, C. (2005), ‘Multiple scattering effects due to hydrometeors on precipitation radar systems’, *Geophys. Res. Lett.* **32**.

Battaglia, A., Muinonen, K., Nousiainen, T. & Peltoniemi, J. I. (1999), ‘Light scattering by Gaussian particles: Rayleigh-ellipsoid approximation’, *JQSRT* **63**, 277–303.

Benincasa, D. S., Barber, P. W., Zhang, J. Z., Hsieh, W. F. & Chang, R. K. (1987), ‘Spatial distribution of the internal and near-field intensities of large cylindrical and spherical scatterers’, *Appl. Opt.* **26**, 1348–1356.

Bohren, C. F. & Huffman, D. R. (1983), *Absorption and scattering of light by small particles*, Wiley, New York.

Bruning, J. H. & Lo, Y. T. (1971), ‘Multiple scattering of EM waves by spheres’, *IEEE Trans. Antennas Propag.* **19**, 378–400.

Cho, H. R., Iribarne, J. V. & Richards, W. G. (1981), ‘On the orientation of ice crystals in a cumulonimbus cloud’, *J. Atmos. Sci.* **38**, 1111–1114.

Chylék, P., Kiehl, J. T., Ko, M. K. W. & Ashkin, A. (1980), Surface waves in light scattering by spherical and non-spherical particles, *in* D. W. Shuerman, ed., ‘Light Scattering by Irregularly Shaped Particles’, Plenum, New York, pp. 153–164.

Chylék, P., Pendleton, J. D. & Pinnick, R. G. (1985), ‘Internal and near-surface scattered field of a spherical particle at resonance conditions’, *Appl. Opt.* **24**, 3940–3942.

Chýlek, P., Videen, G., Geldart, D. J. W., Dobbie, J. S. & Tso, H. C. W. (2000), *Effective-medium approximations for heterogeneous particles*, Academic Press, pp. 273–308.

Debye, P. (1909), ‘Der Lichtdruck auf Kugeln von Beliebigem Material’, *Ann. Phys.* **30**, 57–136.

DeVoe, H. (1964), ‘Optical properties of molecular aggregates. I. Classical model of electronic absorption and refraction’, *J. Chem. Phys.* **41**, 393–400.

Doicu, A., Eremin, Y. A. & Wriedt, T. (1999), ‘Convergence of the T-matrix method for light scattering from a particle on or near a surface’, *Opt. Commun.* **159**, 266–277.

Draine, B. T. (1988), ‘The discrete-dipole approximation and its application to interstellar grains’, *Astrophys. J.* **333**, 848–872.

Draine, B. T. (2008), ‘Discrete-dipole approximation for periodic targets: theory and tests’, *J. Opt. Soc. Am. A* **25**, 2693–2703.

Draine, B. T. & Goodman, J. (1993), ‘Beyond Clausius-Mossotti: Wave propagation on a polarizable point lattice and the discrete-dipole approximation’, *Astrophys. J.* **405**, 685–697.

Fabry, F. & Szyrmer, W. (1999), ‘Modeling of the melting layer. Part II: Electromagnetic’, *J. Atmos. Sci.* **56**, 3593–3600.

Fahlen, T. S. & Bryant, H. C. (1968), ‘Optical back scattering from single water droplets’, *J. Opt. Soc. Am.* **58**(3), 304–310.

Festou, M. C., Rickman, H. & West, R. M. (1993), ‘Comets II. Models, evolution, origin and outlook’, *Astron. Astrophys. Rev.* **5**, 37–163.

Fuller, K. A. (1991), ‘Optical resonances and two-sphere systems’, *Appl. Opt.* **30**(33), 4716–4731.

Gledhill, T. M. & McCall, A. (2000), ‘Circular polarization by scattering from spheroidal dust grains’, *Mon. Not. R. Astron. Soc.* **314**, 123–137.

Goidet-Devel, B., Renard, J. B. & Levasseur-Regourd, A. C. (1995), ‘Polarization of asteroids. Synthetic curves and characteristic parameters’, *Planet Space Sci.* **43**, 779–786.

Göke, S. (1999), Microphysics of the melting layer, PhD thesis, Swiss federal institute of technology.

Hansen, J. E. & Travis, L. D. (1974), ‘Light scattering in planetary atmospheres’, *Space Sci. Rev.* **16**, 527–610.

Helbert, J., Moroz, L. V., Maturilli, A., Bischoff, A., Warell, J., Sprague, A. & Palomba, E. (2007), ‘A set of laboratory analogue materials for the MERTIS instrument on the ESA BebiColombo mission to Mercury’, *Adv. Space Res.* **40**, 272–279.

Hobbs, P. V. (1965), ‘The aggregation of ice crystals in clouds and fogs at low temperatures’, *J. Atmos. Sci.* **22**, 296–300.

Hovenier, J. W. & van der Mee, C. V. M. (2000), Basic relationship for matrices describing scattering by small particles, *in* M. I. Mishchenko, J. W. Hovenier & L. D. Travis, eds, ‘Light scattering by nonspherical particles’, Academic Press, pp. 61–85.

Ishimoto, H. (2008), ‘Radar backscattering computations for fractal-shaped snowflakes’, *J. Meteor. Soc. Japan* **86**(3), 459–469.

Jackson, J. D. (1998), *Classical electrodynamics*, Wiley, New York.

Jenniskens, P. (1993), ‘Optical constants of organic refractory residue’, *Astron. Astrophys.* **274**, 653–661.

Kahnert, F. M., Stamnes, J. J. & Stamnes, K. (2001), ‘Application of the extended boundary condition method to homogeneous particles with point group symmetries’, *Appl. Opt.* **40**, 3110–3123.

Korolev, A. & Isaac, G. (2003), ‘Roundness and aspect ratio of particles in ice clouds’, *J. Atmos. Sci.* **60**, 1795–1808.

Kraus, M. J. (1966), Snowflake aggregation - A numerical model, Master’s thesis, Massachusetts institute of technology.

Laitinen, H. & Lumme, K. (1998), ‘T-matrix method for general star-shaped particles: First results’, *JQSRT* **60**(3), 325–334.

Levasseur-Regourd, A. C., Hadamcik, E. & Renard, J. B. (1996), ‘Evidence for two classes of comets from their polarimetric properties at large phase angles’, *Astron. Astrophys.* **313**, 327–333.

Li, C., Kattawar, G. W. & Zhai, P. W. (2005), ‘Electric and magnetic energy density distributions inside and outside dieletric particles illuminated by a plane electromagnetic wave’, *Opt. Express* **13**, 4554–4559.

Libbrecht, K. G. (2005), ‘The physics of snow crystals’, *Rep. Prog. Phys.* **68**, 855–895.

Lindqvist, H., Muinonen, K. & Nousiainen, T. (2009), ‘Light scattering by coated Gaussian and aggregate particles’, *JQSRT* **110**, 1398–1410.

Lippmann, B. A. (1953), ‘Note on the theory of gratings’, *J. Opt. Soc. Am.* **43**, 408.

Liu, H. & Chandrasekar, V. (2000), ‘Classification of hydrometeors based on polarimetric radar measurements: Development of fuzzy logic and neuro-fuzzy systems, and in situ verification’, *J. Atmos. Oceanic Technol.* **17**, 140–164.

Lorenz, L. V. (1890), ‘Lysbevaegelsen i og uden for en af plane Lysbolger belyst Kugle’, *Det Kongelige Danske Videnskabernes Selskabs Skrifter* **1**, 1–62.

Love, A. E. H. (1899), ‘The scattering of electric waves by a dielectric sphere’, *Proc. Lond. Math. Soc.* **30**, 301–328.

Lumme, K. & Rahola, J. (1994), ‘Light scattering by porous dust particles in the discrete-dipole approximation’, *Astrophys. J.* **425**, 653–667.

Lyot, B. (1929), ‘Recherches sur la polarisation de la lumiére des planétes et de quelques substances terrestres’, *Ann. Obs. Paris* **8**, 1–161.

Mackowski, D. W. & Mishchenko, M. I. (1996), ‘Calculation of the T matrix and the scattering matrix for ensembles of spheres’, *J. Opt. Soc. Am. A* **13**(11), 2266–2278.

Magono, C. & Lee, C. W. (1966), ‘Meteorological classification of natural snow crystals’, *J. Fac. Sci., Hokkaido Univ., Series VII* **2**, 321–362.

Mallama, A., Wang, D. & Howard, R. A. (2002), ‘Photometry of Mercury from SOHO/LASCO and Earth: The phase function from 2 to 170°’, *Icarus* **155**, 253–264.

Maruyama, K. & Fujiyoshi, Y. (2005), 'Monte Carlo simulation of the formation of snowflakes', *J. Atmos. Sci.* **62**, 1529–1544.

Matrosov, S. Y. (1998), 'Dual wavelength radar method to measure snowfall rate', *J. Appl. Meteor.* **37**, 1510–1521.

McIlveen, J. F. R. (1992), *Fundamentals of weather and climate*, Chapman & Hall, London.

McKay, D. S., Carter, J. L., Boles, W. W., Allen, C. C. & Allton, J. H. (1993), A new lunar regolith simulant, *in* 'Twenty-Fourth Lunar and Planetary Science Conference, Houston, Texas'.

Meneghini, R. & Liao, L. (2000), 'Effective dielectric constants of mixed-phase hydrometeors', *J. Atmos. Oceanic Technol.* **17**, 628–640.

Mie, G. (1908), 'Beiträge zur Optik trÃijber Medien, speziell kolloidaler Metallösungen', *Ann. Phys.* **330**, 377–445.

Mishchenko, M. I. (1991), 'Light scattering by randomly oriented axially symmetric particles', *J. Opt. Soc. Am. A* **8**, 871–882.

Mishchenko, M. I. (1993), 'On the nature of the polarization opposition effect exhibited by Saturn's rings', *Astrophys. J.* **411**, 351–361.

Mishchenko, M. I. (2000), 'Calculation of the amplitude matrix for a nonspherical particle in a fixed orientation', *Appl. Opt.* **39**, 1026–1031.

Mishchenko, M. I., Tishkovets, V. P., Travis, L. D., Cairns, B., Dlugach, J. M., Liu, L., Rosenbush, V. K. & Kiselev, N. N. (2011), 'Electromagnetic scattering by a morphologically complex object: Fundamental concepts and common misconceptions', *JQSRT* **112**, 671–692.

Muinonen, K. (1990), Light scattering by inhomogeneous media: Backward enhancement and reversal of polarization, PhD thesis, University of Helsinki.

Muinonen, K. (1996), 'Light scattering by Gaussian random particles', *Earth Moon Planets* **72**, 339–342.

Muinonen, K. (1998), 'Introducing the Gaussian shape hypothesis for asteroids and comets', *Astron. Astrophys.* **332**, 1087–1098.

Muinonen, K., Nousiainen, T., Fast, P., Lumme, K. & Peltoniemi, J. (1996), 'Light scattering by Gaussian random particles: Ray optics approximation', *JQSRT* **55**, 577–601.

Muinonen, K., Tyynelä, J., Zubko, E. & Videen, G. (2010), 'Scattering parameterization for interpreting asteroid polarimetric and photometric phase effects', *Earth Planets Space* **62**, 47–52.

Muinonen, K. & Zubko, E. (2010), Coherent backscattering by a finite medium of particles, *in* K. Muinonen, A. Penttilä, H. Lindqvist, T. Nousiainen & G. Videen, eds, 'Proceedings of the 12th Conference on Electromagnetic and Light Scattering by Nonspherical Particles', pp. 194–197.

Muinonen, K., Zubko, E., Shkuratov, Y. G. & Videen, G. (2006), Discrete-dipole light-scattering simulations for Gaussian particles with power-law covariance, *in* N. Voshchinnikov, ed., 'Proceedings of the 9th Conference on Electromagnetic and Light Scattering by Nonspherical Particles: Theory, Measurements and Applications', pp. 207–210.

Muinonen, K., Zubko, E., Tyynelä, J., Shkuratov, Y. G. & Videen, G. (2007), 'Light scattering by Gaussian random particles with discrete-dipole approximation', *JQSRT* **106**, 360–377.

Muñoz, O., Volten, H., de Haan, J. F. & Vassen, W. (2001), 'Experimental determination of scattering matrices of randomly oriented fly ash and clay particles at 442 and 633 nm', *J. Geophys. Res.* **106**, 22833–22844.

Nakamura, R. & Okamoto, H. (1999), 'Optical properties of fluffy aggregates as analogue of interplanetary dust particles', *Adv. Space Res.* **23**, 1209–1212.

Nakaya, U. (1954), *Snow crystals: natural and artificial*, Harvard university press.

Nousiainen, T., Kahnert, M. & Lindqvist, H. (2011), 'Can particle shape information be retrieved from light-scattering observations using spheroidal model particles?', *JQSRT* **112**, 2213–2225.

Nousiainen, T. & McFarquhar, G. (2004), 'Light scattering by quasi-spherical ice crystals', *J. Atmos. Sci.* **61**(18), 2229–2248.

Nousiainen, T., Muñoz, O., Lindqvist, H., Mauno, P. & Videen, G. (2011), 'Light scattering by large Saharan dust particles: Comparison of modeling and experimental data for two samples', *JQSRT* **112**, 420–433.

Owen, J. F., Chang, R. K. & Barber, P. W. (1981), 'Internal electric field distributions of a dielectric cylinder at resonance wavelengths', *Opt. Lett.* **6**, 540–542.

Pauling, L. (1935), 'The structure and entropy of ice and of other crystals with some randomness of atomic arrangement', *J. Am. Chem. Soc.* **57**, 2680–2684.

Penttilä, A., Zubko, E., Lumme, K., Muinonen, K., Yurkin, M. A., Draine, B., Rahola, J., Hoekstra, A. G. & Shkuratov, Y. (2007), 'Comparison between discrete dipole implementations and exact techniques', *JQSRT* **106**, 417–436.

Peterson, B. & Ström, S. (1973), 'T matrix for electromagnetic scattering from an arbitrary number of scatterers and representations of E(3)*', *Phys. Rev. D* **8**, 3661–3678.

Petrov, D., Shkuratov, Y. G. & Videen, G. (2011), 'Electromagnetic wave scattering from particles of arbitrary shapes', *JQSRT* **112**, 1636–1645.

Petrova, E. V., Jockers, K. & Kiselev, N. N. (2000), 'Light scattering by aggregates with sizes comparable to the wavelength: An application to cometary dust', *Icarus* **148**, 526–536.

Pluchino, A. B. (1981), 'Surface waves and the radiative properties of micron-sized particles', *Appl. Opt.* **20**, 2986–2992.

Probert-Jones, J. R. (1984), 'Resonance component of backscattering by large dielectric spheres', *J. Opt. Soc. Am. A* **1**(8), 822–830.

Pruppacher, H. R. & Klett, J. D. (1997), *Microphysics of clouds and precipitation*, Dordrecht, Boston.

Purcell, E. M. & Pennypacker, C. R. (1973), 'Scattering and absorption of light by nonspherical dielectric grains', *Astrophys. J.* **186**, 705–714.

Ren, K. F. (1994), 'Symmetry relations in generalized Lorenz-Mie theory', *J. Opt. Soc. Am. A* **11**, 1812–1817.

Rosenbush, V. K. & Kiselev, N. N. (2005), 'Polarization opposition effect for the Galilean satellites of Jupiter', *Icarus* **179**, 490–496.

Russchenberg, H. W. J. & Ligthart, L. P. (1996), 'Backscattering by and propagation through the melting layer of precipitation: A new polarimetric model', *IEEE Trans. Geosci. Remote Sens.* **34**(1), 3–14.

Ryde, J. W. (1946), 'Attenuation of centimeter radio waves and echo intensities resulting from atmospheric phenomena', *J. IEEE* **93**(3), 101–103.

Samson, R. J., Mulholland, G. W. & Gentry, J. W. (1987), 'Structural analysis of soot aggregates', *Langmuir* **3**, 272–281.

Schmidt, V. & Wriedt, T. (2009), 'T-matrix method for biaxial anisotropic particles', *JQSRT* **110**, 1392–1397.

Schmitt, C. G. & Heymsfield, A. J. (2010), 'The dimensional characteristics of ice crystal aggregates from fractal geometry', *J. Atmos. Sci.* **67**(5), 1605–1616.

Shibkov, A. A., Golovin, Y. I., Zheltov, M. A., Korolev, A. A. & Leonov, A. A. (2003), 'Morphology diagram of nonequilibrium patterns of ice crystals growing in supercooled water', *Physica A* **319**, 65–79.

Shkuratov, Y. G. (1989), 'A new mechanism of the negative polarization of light scattered by the surfaces of atmosphereless celestial bodies', *Astron. Vestn.* **23**, 176–180.

Shkuratov, Y. G., Opanasenko, N. V. & Kreslavsky, M. A. (1992), 'Polarimetric and photometric properties of the Moon: Telescopic observations and laboratory simulations: 1. The negative polarization', *Icarus* **95**, 283–299.

Shkuratov, Y. G., Ovcharenko, A., Zubko, E., Miloslavskaya, O., Muinonen, K., Piironen, J., Nelson, R., Smythe, W., Rosenbush, V. & Helfenstein, P. (2002), 'The opposition effect and negative polarization of structural analogs for planetary regoliths', *Icarus* **159**, 396–416.

Sihvola, A. (1989), 'Self-consistency aspects of dielectric mixing theories', *IEEE Trans. Geosci. Remote Sens.* **27**, 403–415.

Smyth, T. J. & Illingworth, A. J. (1998), 'Radar estimates of rainfall rates at the ground in bright band and non-bright band events', *Quart. J. Roy. Meteor. Soc.* **124**, 2417–2434.

Straka, J. M., Zrnić, D. S. & Ryzhkov, A. V. (2000), 'Bulk hydrometeor classification and quantification using polarimetric radar data: Synthesis of relations', *J. Appl. Meteor.* **39**, 1341–1372.

Teschl, F. & Randeu, W. L. (2009), The DDA for modeling the scattering of radar waves by liquid an frozen precipitation particles, *in* 'Proceedings of the DDA-workshop, Bremen, Germany', pp. 25–29.

Ulaby, F. T. & Elachi, C. (1990), *Radar polarimetry for geoscience applications*, Artech House, Boston.

van de Hulst, H. C. (1957), *Light scattering by small particles*, Wiley, New York.

Veihelmann, B., Nousiainen, T., Kahnert, M. & van der Zande, W. J. (2006), 'Light scattering by small feldspar particles simulated using the Gaussian random sphere geometry', *JQSRT* **100**, 393–405.

Visser, H. J. (2005), *Array and phased array antenna basics*, Wiley.

Waterman, P. C. (1965), 'Matrix formulation of electromagnetic scattering', *Proc. IEEE* **53**, 805–812.

Westbrook, C. D. (2004), Universality in snow formation, PhD thesis, University of Warwick.

Westbrook, C. D., Ball, R. C. & Field, P. R. (2006), 'Radar scattering by aggregate snowflakes', *Q. J. R. Meteorol. Soc.* **132**(616), 897–914.

Wiscombe, W. J. (1980), 'Improved Mie scattering algorithms', *Appl. Opt.* **19**(9), 1505–1509.

Wriedt, T. (2007), 'Review of the null-field method with discrete sources', *JQSRT* **106**, 535–545.

Wriedt, T. & Doicu, A. (1997), 'Comparison between various formulations of the extended boundary condition method', *Opt. Commun.* **142**, 91–98.

Yanamandra-Fisher, P. A. & Hanner, M. S. (1999), 'Optical properties of nonspherical particles of size comparable to the wavelength of light: Application to comet dust', *Icarus* **138**, 107–128.

Yang, P. & Liou, K. N. (1996), 'Finite-difference time domain method for light scattering by small ice crystals in three-dimensional space', *J. Opt. Soc. Am. A* **13**, 2072–2085.

Yurkin, M. A. & Hoekstra, A. G. (2007), 'The discrete-dipole approximation: An overview and recent developments', *JQSRT* **106**, 558–589.

Yurkin, M. A. & Hoekstra, A. G. (2011), 'The discrete-dipole-approximation code ADDA: Capabilities and known limitations', *JQSRT* **112**, 2234–2247.

Yurkin, M. A., Maltsev, V. P. & Hoekstra, A. G. (2006), 'Convergence of the discrete-dipole approximation. I. Theoretical analysis', *J. Opt. Soc. Am. A* **23**, 2578–2591.

Yurkin, M. A., Min, M. & Hoekstra, A. G. (2010), 'Application of the discrete-dipole approximation to very large refractive indices: Filtered coupled dipoles revived', *Phys. Rev. E* **82**.

Zubko, E., Kimura, H., Shkuratov, Y. G., Muinonen, K., Yamamoto, T., Okamoto, H. & Videen, G. (2009), 'Effect of absorption on light scattering by agglomerated-debris particles', *JQSRT* **110**, 1741–1749.

Zubko, E., Muinonen, K., Shkuratov, Y. G., Videen, G. & Nousiainen, T. (2007), 'Scattering of light by roughened Gaussian random particles', *JQSRT* **106**, 604–615.

Zubko, E., Petrov, D., Grynko, Y., Shkuratov, Y. G., Okamoto, H., Muinonen, K., Nousiainen, T., Kimura, H., Yamamoto, T. & Videen, G. (2010), 'Validity criteria of the discrete-dipole approximation', *Appl. Opt.* **49**, 1267–1279.

Zubko, E., Petrov, D., Shkuratov, Y. G. & Videen, G. (2005), 'Discrete-dipole approximation simulations of scattering by particles with hierarchical structure', *Appl. Opt.* **44**, 6479–6485.

Zubko, E., Shkuratov, Y. G. & Videen, G. (2006), 'Discrete-dipole analysis of backscatter features of agglomerated debris particles comparable in size with wavelength', *JQSRT* **100**, 483–488.